

1 **Long-term trends of ambient nitrate (NO<sub>3</sub><sup>-</sup>) concentrations across China based on ensemble**  
2 **machine-learning models**

3 Rui Li<sup>a</sup>, Lulu Cui<sup>a\*</sup>, Yilong Zhao<sup>a</sup>, Wenhui Zhou<sup>a</sup>, Hongbo Fu<sup>a,b,c\*</sup>

4 <sup>a</sup> Shanghai Key Laboratory of Atmospheric Particle Pollution and Prevention, Department of  
5 Environmental Science & Engineering, Institute of Atmospheric Sciences, Fudan University,  
6 Shanghai, 200433, P.R. China

7 <sup>b</sup> Collaborative Innovation Center of Atmospheric Environment and Equipment Technology  
8 (CICAET), Nanjing University of Information Science and Technology, Nanjing 210044, P.R.  
9 China

10 <sup>c</sup> Shanghai Institute of Pollution Control and Ecological Security, Shanghai 200092, P.R. China

11 \* Correspondence to:

12 Drs. H. Fu (Email: [fuhb@fudan.edu.cn](mailto:fuhb@fudan.edu.cn)) and L. Cui (Email: 15110740004@fudan.edu.cn)

13 **Abstract**

14 High loadings of nitrate (NO<sub>3</sub><sup>-</sup>) in the aerosol over China significantly exacerbates the air quality  
15 and poses a great threaten on ecosystem safety through dry/wet deposition. Unfortunately, limited  
16 ground-level observation data makes it challenging to fully reflect the spatial pattern of NO<sub>3</sub><sup>-</sup> level  
17 across China. Up to date, the long-term monthly particulate NO<sub>3</sub><sup>-</sup> datasets at a high resolution were  
18 still missing, which restricted the assessment of human health and ecosystem safety. Therefore, a  
19 unique monthly NO<sub>3</sub><sup>-</sup> dataset at 0.25 ° resolution over China during 2005-2015 was developed by  
20 assimilating surface observation, satellite product, meteorological data, land use types and other  
21 covariates using an ensemble model combining random forest (RF), gradient boosting decision tree  
22 (GBDT), and extreme gradient boosting (XGBoost). The new developed product featured excellent  
23 cross-validation R<sup>2</sup> value (0.78) and relatively lower root-mean-square error (RMSE: 1.19  $\mu\text{g}/\text{m}^3\mu\text{g}$   
24  $\text{N m}^{-3}$ ) and mean absolute error (MAE: 0.81  $\mu\text{g}/\text{m}^3\mu\text{g N m}^{-3}$ ). Besides, the dataset also exhibited

带格式的: 上标

带格式的: 上标

25 relatively robust performance at the spatial and temporal scale. Moreover, the dataset displayed  
26 good agreement with ( $R^2 = 0.85$ ,  $RMSE = 0.74 \mu\text{g}/\text{m}^3$ , and  $MAE = 0.55 \mu\text{g}/\text{m}^3$ )  
27 some unlearned data collected from previous studies. The spatiotemporal variations of the  
28 developed product were also shown. The estimated  $\text{NO}_3^-$  concentration showed the highest value in  
29 North China Plain (NCP) ( $3.55 \pm 1.25 \mu\text{g}/\text{m}^3$ ), followed by Yangtze River Delta (YRD  
30 ( $2.56 \pm 1.12 \mu\text{g}/\text{m}^3$ ), Pearl River Delta (PRD ( $1.68 \pm 0.81 \mu\text{g}/\text{m}^3$ )), Sichuan Basin  
31 ( $1.53 \pm 0.63 \mu\text{g}/\text{m}^3$ ), and the lowest one in Tibetan Plateau ( $0.42 \pm 0.25 \mu\text{g}/\text{m}^3$ ).  
32 The higher ambient  $\text{NO}_3^-$  concentrations in NCP, YRD, and PRD were closely linked to the dense  
33 anthropogenic emissions. Apart from the intensive human activities, poor terrain condition might  
34 be a key factor for the serious  $\text{NO}_3^-$  pollution in Sichuan Basin. The lowest ambient  $\text{NO}_3^-$   
35 concentration in Tibetan Plateau was contributed by the scarce anthropogenic emission and  
36 favorable meteorological factors (e.g., high wind speed). In addition, the ambient  $\text{NO}_3^-$   
37 concentration showed marked increasing tendency of  $0.10 \mu\text{g}/\text{m}^3/\text{year}$  during 2005-2014  
38 ( $p < 0.05$ ), while it decreased sharply from 2014 to 2015 at a speed of  $-0.40 \mu\text{g}/\text{m}^3/\text{year}$  ( $p$   
39  $< 0.05$ ). The ambient  $\text{NO}_3^-$  levels in Beijing-Tianjin-Hebei (BTH), YRD, and PRD displayed gradual  
40 increases at the speed of 0.20, 0.11, and  $0.05 \mu\text{g}/\text{m}^3/\text{year}$  ( $p < 0.05$ ) during 2005-2013,  
41 respectively. The gradual increases of  $\text{NO}_3^-$  concentrations in these regions from 2005 to 2013 were  
42 due to that the emission reduction measures during this period focused on the reduction of  $\text{SO}_2$   
43 emission rather than  $\text{NO}_x$  emission and the rapid increase of energy consumption. Afterwards, the  
44 government further strengthened these emission reduction measures, and thus caused the dramatic  
45 decreases of  $\text{NO}_3^-$  concentrations in these regions from 2013 to 2015 ( $p < 0.05$ ). The long-term  $\text{NO}_3^-$   
46 dataset over China could greatly deepen the knowledge about the impacts of emission reduction

带格式的: 上标

带格式的: 上标

带格式的: 上标

带格式的: 上标

带格式的: 上标

带格式的: 上标

带格式的: 上标

带格式的: 上标

带格式的: 上标

带格式的: 上标

47 measures on air quality improvement. The monthly particulate  $\text{NO}_3^-$  levels over China during 2005-  
48 2015 are open access in <https://doi.org/10.5281/zenodo.3988307> (Li et al., 2020c).

## 49 **1. Introduction**

50 Reactive nitrogen ( $\text{N}_r$ ) emissions displayed remarkable increases in the past decades owing to  
51 the high-speed industrial development and urbanization (Cui et al., 2016; Singh et al., 2017).  
52 Ambient reactive N emissions were mainly characterized with nitrogen oxides ( $\text{NO}_x$ ), accounting  
53 for about 30% of the gross  $\text{N}_r$  emissions (Chen et al., 2015; Liu et al., 2011). These important N-  
54 bearing precursors could be transformed into the nitrate ( $\text{NO}_3^-$ ) via multiple chemical pathways (e.g.,  
55 heterogeneous or liquid phase reaction), and finally deposited in the terrestrial or aquatic ecosystem  
56 (Jia et al., 2016; Qiao et al., 2015; Zhao et al., 2017). On the one hand, heavy loadings of  $\text{NO}_3^-$   
57 greatly degraded the atmospheric visibility and cool the surface of the Earth system because  
58 particulate  $\text{NO}_3^-$  significantly scattered solar radiation (Fu and Chen, 2017). Moreover, enhanced N  
59 deposition might pose a negative effect on the ecosystem health such as biodiversity losses,  
60 freshwater eutrophication, and oceanic acidification (Compton et al., 2011; Erismann et al., 2013).  
61 Hence, deepening the knowledge about the spatial patterns and long-term trends of particulate  $\text{NO}_3^-$   
62 in the atmosphere is beneficial to accurately evaluate the ecological and environmental effects of N  
63 deposition.

64 Ground-level observation is often acknowledged to be an effective means to explore the spatial  
65 patterns of ambient  $\text{NO}_3^-$  concentrations. Many long-term monitoring networks including Clean Air  
66 Status and Trends Network (CASTNET) and Canadian Air and Precipitation Monitoring Network  
67 (CAPMoN) were established to quantify the ambient  $\text{NO}_3^-$  concentration and inorganic N deposition.  
68 Du et al. (2014) revealed that the  $\text{NO}_3^-$  deposition showed significant decrease across the United

69 States during 1985-2012 based on these observation data. To date, most of these observation  
70 networks focused on North America and Europe, whereas few monitoring sites were located on East  
71 Asia especially on China. Fortunately, China has constructed some ground-level observation  
72 networks such as CARE-China Observation Network in recent years. On the basis of these  
73 observation networks, the overall spatiotemporal trend of particulate  $\text{NO}_3^-$  concentration has been  
74 clarified (Wang et al., 2019c; Xu et al., 2018a). Xu et al. (2018a) observed that the particulate  $\text{NO}_3^-$   
75 concentration ( $< 4.5 \mu\text{m}$ ) over China did not show significantly temporal variation during 2011-  
76 2015. Very recently, Wang et al. (2019) found that the  $\text{NO}_3^-$  level in the fine particle ( $\text{PM}_{2.5}$ )  
77 decreased by 34% during 2015-2017. Although the overall spatial patterns have been preliminarily  
78 revealed based on these isolated sites, these sparse ground-observed sites ~~did not accurately might~~  
79 ~~not~~ reflect the high-resolution  $\text{NO}_3^-$  pollution ~~across China~~ especially the regions far away from these  
80 sites because each station only possessed limited spatial representative and  $\text{NO}_3^-$  concentration was  
81 often highly variable in space and time (Liu et al., 2017a). More importantly, the current studies  
82 only investigated the ambient  $\text{NO}_3^-$  concentrations in recent years, while the long-term variation of  
83  $\text{NO}_3^-$  level remained unknown. It was well known that the energy consumption in China displayed  
84 remarkable increase in recent decades (Zhan et al., 2018). Meanwhile, Chinese government also  
85 proposed pollutant emission reduction policies since 2005 to ensure the coordinated development  
86 of economic growth and environmental protection (Ma et al., 2019). However, the synergistic effects  
87 of air pollution control policies and increased energy consumption on long-term evolution trend of  
88  $\text{NO}_3^-$  pollution over China were not assessed yet, which were extremely critical for the  
89 implementation of emission control measures.

90 To complement the gaps of ground-level observations, satellite product of  $\text{NO}_2$  is regarded as a

91 welcome addition to investigate the long-term trends of N-bearing components in the atmosphere.  
92 Ozone Monitoring Instrument (OMI) was regarded as the typical satellite product applied to  
93 simulate the ambient  $\text{NO}_3^-$  concentration (Liu et al., 2017b; Vrekoussis et al., 2013). Jia et al. (2016)  
94 firstly used the linear regression method to predict the  $\text{NO}_3^-$  levels and dry deposition fluxes at the  
95 global scale based on OMI-derived  $\text{NO}_2$  column amount. However, the dry deposition fluxes of  
96  $\text{NO}_3^-$  modelled by Jia et al. (2016) showed weak correlation with the measured value ( $R = 0.47$ ),  
97 which might be attributable to the simple linear assumption between  $\text{NO}_2$  column amount and  $\text{NO}_3^-$   
98 deposition flux. It was well documented that the nonlinearity relationship between multiple  
99 predictors and  $\text{NO}_3^-$  concentration were hard to reveal on the basis of the simple linear model (Zhan  
100 et al., 2018a; Zhan et al., 2018b). To enhance the predictive performance of  $\text{NO}_3^-$  concentration, Liu  
101 et al. (2017) used the chemical transport models (CTMs) to estimate the dry deposition fluxes of N-  
102 bearing species recently based on the remotely sensed  $\text{NO}_2$  column amount. However, CTMs often  
103 suffered from high uncertainty because of the limited knowledge about the generation pathways for  
104 particulate  $\text{NO}_3^-$  in the atmosphere (Zhan et al., 2018a). Recently, the emergence of machine  
105 learning models provided unprecedented opportunities to estimate the concentrations of N-bearing  
106 components (Chen et al., 2019b; Zhan et al., 2018b). It was well known that the machine-learning  
107 models generally showed the better predictive accuracy than CTMs and traditional statistical models  
108 when the training samples were sufficient (Zang et al., 2019; Zhan et al., 2017). ~~In the pioneering~~  
109 ~~studies, the  $\text{NO}_2$  estimation has aroused widespread concern (Zhan et al., 2018b; Chen et al., 2019).~~  
110 Zhan et al. (2018b) employed random forest (RF) coupled with spatiotemporal Kriging model to  
111 simulate the ambient  $\text{NO}_2$  levels over China, and achieved the moderate modelling performance ( $R^2$   
112 = 0.62). Afterwards, Chen et al. (2019) used the extreme gradient boosting (XGBoost) model

113 combined with kriging-calibrated satellite method to estimate the national NO<sub>2</sub> concentration and  
114 significantly improved the predictive performance ( $R^2 = 0.85$ ). Up to date, no study utilized the  
115 machine-learning models to significantly improve the predictive accuracy of NO<sub>3</sub><sup>-</sup> concentration.  
116 Moreover, nearly all of the current studies only focused on the spatial pattern of particulate NO<sub>3</sub><sup>-</sup>  
117 level in China (Liu et al., 2017; Jia et al., 2016), while they cannot establish a long-term NO<sub>3</sub><sup>-</sup> dataset  
118 across China.

119 Here, we firstly developed a high-resolution (0.25°) monthly particulate NO<sub>3</sub><sup>-</sup> dataset across  
120 China during 2005-2015 based an ensemble model including RF, XGBoost, and gradient boosting  
121 decision tree (GBDT) algorithms. At first, the modelling performance and improvement of this new-  
122 developed product compared with previous datasets were evaluated. Afterwards, we analyzed the  
123 spatial variation and long-term evolution trend of estimated NO<sub>3</sub><sup>-</sup> concentration over China and  
124 explored the potential impacts of air pollution control measures on NO<sub>3</sub><sup>-</sup> variation. The long-term  
125 NO<sub>3</sub><sup>-</sup> datasets could supply scientific judge for policy makers to mitigate the severe nitrate pollution  
126 in China.

## 127 **2. Input data**

### 128 2.1 Ground-level NO<sub>3</sub><sup>-</sup> data

129 The monthly NO<sub>3</sub><sup>-</sup> monitoring data during 2010-2015 were collected from nationwide nitrogen  
130 deposition monitoring network (NNDMN) including 32 sites (Fig. 1, Fig. S1, and Fig. S2), and  
131 these sites could be divided into three types including urban, rural, and background sites (Xu et al.,  
132 2018a). Ambient concentrations of particulate NO<sub>3</sub><sup>-</sup> were determined on the basis of an active  
133 DEnuder for Long-Term Atmospheric sampling system (DELTA) (~~DEnuder for Long-Term~~  
134 ~~Atmospheric sampling) system. The system comprises of a pump, a filter sampling instrument, and~~

135 a dry gas meter with high sensitivity. Two set of filters in a 2-stage filter pack was applied to sample  
136 the aerosol particles, with a first K<sub>2</sub>CO<sub>3</sub>/glycerol impregnated filter to obtain NO<sub>3</sub><sup>-</sup> particles in PM<sub>10</sub>.  
137 All of the monitoring sites kept the same sampling frequency at the month scale, and these samples  
138 were continuously collected over a month. The detailed sampling and analysis procedures have been  
139 described by Xu et al. (2018a) and Xu et al. (2019). The detection limit of particulate NO<sub>3</sub><sup>-</sup>  
140 concentration over China is 0.05-01 mg N/L.

#### 141 2.2 Satellite product of NO<sub>2</sub> column density

142 The OMI-NO<sub>2</sub> level-3 tropospheric column densities (0.25° resolution) were used to predict the  
143 NO<sub>3</sub><sup>-</sup> concentration (Fig. S3). The OMI aboard on the Aura satellite was available since September,  
144 2004, which displayed global coverage and crossed the entire earth each day. OMI possessed three  
145 spectral channels ranging from 270 to 500 nm, and thus was often applied to monitor the gaseous  
146 pollutants such as NO<sub>2</sub>, SO<sub>2</sub>, and O<sub>3</sub>.

147 In this study, we downloaded the daily NO<sub>2</sub> columns during 2005-2015 from  
148 <https://earthdata.nasa.gov/>. The tropospheric NO<sub>2</sub> column density data of poor quality (e.g., cloud  
149 radiance fraction > 0.5, solar zenith angles > 85°, and terrain reflectivity > 30%) should be removed.  
150 Additionally, the cross-track pixels sensitive to significant row anomaly also must be deleted.  
151 Finally, the monthly NO<sub>2</sub> columns were estimated by averaging the daily NO<sub>2</sub> columns.

#### 152 2.3 Meteorological factors, land use types, and other variables

153 These independent variables for particulate NO<sub>3</sub><sup>-</sup> estimates were gained from multiple sources.  
154 The meteorological data on a daily basis (European Centre for Medium-Range Weather Forecasts  
155 reanalysis (ECMWF ERA-Interim) datasets (0.25° resolution)) were downloaded from ~~in~~ the  
156 website of <http://www.ecmwf.int/> (Table S1). Among all of the daily meteorological data in

157 ECMWF website, 2-m temperature ( $T_{2m}$ ), 2-m dewpoint temperature ( $D_{2m}$ ), 10-m latitudinal wind  
158 wind component ( $U_{10}$ ), 10-m meridional windwind component ( $V_{10}$ ), sunshine duration (Sund),  
159 surface pressure (Sp), boundary layer height (BLH), and total precipitation (Tp) were applied to  
160 estimate national  $NO_3^-$  levels. The elevation, gross domestic production (GDP), and population  
161 density (PD) data over China were downloaded from the website of <http://www.resdc.cn/>. PD and  
162 GDP in 1995, 2000, 2005, 2010, and 2015 were linearly interpolated to calculate PD and GDP in  
163 each year. Then, the yearly GDP data were divided by 12 to estimate the monthly GDP. Afterwards,  
164 these data were incorporated into the final-sub-model to predict the particulate  $NO_3^-$  concentration  
165 over China. In addition, the land use data (e.g., grassland, forest, urban, and agricultural land) were  
166 also downloaded from the website of <http://www.resdc.cn/>.

167 These independent variables collected from various sources were uniformly resampled to  $0.25^\circ$   
168  $\times 0.25^\circ$  grids. For instance, the land use area, GDP, and PD in  $0.25^\circ$  grid was calculated based on  
169 area-weighted average algorithm. To ensure the better predictive performance, it was necessary to  
170 employ the appropriate variable selection method to remove some redundant predictors. The basic  
171 principle of the variable choice was to remove the variables with the lower importance values. The  
172 variables could be regarded as the redundant ones when the  $R^2$  value of the final model showed  
173 dramatic decrease after removing them. Based on this method, in the final sub-model, all of the  
174 variables except GDP, PD, and grassland have been applied to estimate the ambient  $NO_3^-$   
175 concentrations across China.

### 176 3. Methods

#### 177 3.1 Ensemble model development

178 In the previous studies concerning about air pollution prediction, RF, gradient boosting decision

带格式的: 下标

带格式的: 上标

带格式的: 下标

带格式的: 上标



179 tree (GBDT), and extreme gradient boosting (XGBoost) showed good predictive performance (Li  
 180 et al., 2020a). RF model possesses a large amount of decision trees, and each one suffered from an  
 181 independent sampling process and these trees displayed the same distribution (Breiman, 2001). This  
 182 model generally shows the higher prediction accuracy due to the injected randomness. The model  
 183 performance mainly relies on the number of trees, the variable group, and the splitting features. The  
 184 detailed algorithms are shown as follows:

$$185 \quad f(x) = \sum_{z=1}^Z c_z I(x \in M_z) \quad (1)$$

$$186 \quad \hat{c}_z = \text{mean}(y_i | x_i \in M_z) \quad (2)$$

$$187 \quad L_1(m, n) = \{X | X_j \leq n\} \& L_2(m, n) = \{X | X_j > n\} \quad (3)$$

$$188 \quad \min_{m, n} \left[ \min_{M_1(m, n)} \sum (y - c_1)^2 + \min_{M_2(m, n)} \sum (y - c_2)^2 \right] \quad (4)$$

$$189 \quad \hat{c}_1 = \text{mean}(y_i | x_i \in M_1(m, n)) \& \hat{c}_2 = \text{mean}(y_i | x_i \in M_2(m, n)) \quad (5)$$

190 where  $(x_i, y_i)$  denotes the sample for  $i = 1, 2, \dots, N$  in  $M$  regions  $(M_1, M_2, \dots, M_z)$ ;  $I$  denotes  
 191 the weight of each branch;  $L$  denotes the branch of decision tree;  $c_m$  represents the response to the  
 192 model;  $\hat{c}_z$  denotes the best value,  $m$  represents the feature variable;  $c_1$  denotes the mean value  
 193 of left branch;  $c_2$  denotes the mean value of right branch;  $n$  is the split point.

194 GBDT model is often considered to be a typical boosting method. Compared with RF model,  
 195 each classifier is applied to decrease the residual of the last round. The detailed equations are as  
 196 follows:

$$197 \quad c_{ij} = \arg \min \sum_{x_i \in R_{ij}} L(y_i, f_{i-1}(x_i) + c) \quad (6)$$

$$198 \quad f_i(x) = f_{i-1}(x) + \sum_{j=1}^J c_{ij} I \quad (7)$$

带格式的: 下标

199  $c_{ij}$  denotes the predicted the estimation error in the last round;  $R_{ij}$  denotes each leaf node for the  
200 decision trees;  $y_i$  represents the observed value;  $f_{t-1}(x_i)$  is the predicted value in the last round.  $c$  was  
201 regarded as the optimal value when  $c_{ij}$  reaches the least value.

202 XGBoost method is an updated version of GBDT model and loss functions are expanded to the  
203 second order function. On the basis of the pioneering studies (Chen et al., 2019a), XGBoost  
204 generally shows excellent performance because of its high efficiency and impressive accuracy. The  
205 detailed XGBoost algorithm is shown as the following formula (Zhai and Chen, 2018):

$$206 \quad L^{(t)} = \sum_{i=1}^n [l(y_i, y^{\wedge(t-1)}) + \partial_{y^{\wedge(t-1)}} l(y_i, y^{\wedge(t-1)}) f_t(x_i) + \frac{1}{2} \partial_{y^{\wedge(t-1)}}^2 l(y_i, y^{\wedge(t-1)}) f_t^2(x_i)] + \Omega(f_t) \quad (8)$$

207 where  $L^{(t)}$  represents the cost function at the  $t$ -th period;  $\partial$  denotes the derivative of the function;  
208  $\partial_{y^{\wedge(t-1)}}^2$  denotes the second derivative of the function;  $l$  is the differentiable convex loss function that  
209 reveals the difference of the predicted value ( $y^{\wedge}$ ) of the  $i$ -th instance at the  $t$ -th period and the target  
210 value ( $y_i$ );  $f_t(x)$  denotes the increment;  $\Omega(f_t)$  represents the regularizer.

211 However, each model still shows some disadvantages in the prediction accuracy. Consequently,  
212 it was proposed to combine these models with multiple linear regression (MLR) model to further  
213 estimate monthly  $\text{NO}_3^-$  concentration in the atmosphere over China. As shown in Fig. 2, three  
214 submodels including RF, GBDT, and XGBoost were stacked through MLR model to estimate the  
215 monthly  $\text{NO}_3^-$  concentration over China. At first, a 5-fold cross-validation method was adopted to  
216 train each submodel to determine the appropriate parameter. Afterwards, the MLR model was  
217 trained with the final simulated concentrations of three submodels and observations. Finally, the  
218 high-resolution ambient  $\text{NO}_3^-$  level over China were estimated based on the optimal ensemble model.  
219 The detailed algorithms are shown as follows (Fig. 2):

220 
$$NO_3^- = A \times \text{Pred\_RF} + B \times \text{Pred\_GBDT} + C \times \text{Pred\_XGBoost} + e_{ij} \quad (9)$$

221 where Pred\_RF, Pred\_GBDT, and Pred\_XGBoost denote the predicted NO<sub>3</sub><sup>-</sup> concentrations by RF,  
222 GBDT, and XGBoost, respectively. A, B, and C represent the partial regression coefficients of RF,  
223 GBDT, and XGBoost predictors, respectively. *e<sub>ij</sub>* denotes the residual error. Based on the estimates,  
224 the regression coefficients including A, B, C, and the residual error (*e<sub>ij</sub>*) determined by the MLR  
225 model were 0.42, 0.77, 0.09, and -0.87, respectively. The variance inflation factors of RF (2.01),  
226 GBDT (2.69), and XGBoost (2.08) were significantly lower than 10, which suggested the MLR  
227 model was robust.

带格式的: 下标

228 The RF model was trained using matlab2019a with a package named random forest-master. Both  
229 of GBDT and XGBoost algorithms were conducted using many packages named *gbm*, *caret*, and  
230 *xgboost* in R software.

### 231 3.2 The error estimation and uncertainty assessment

232 The estimation performance of the ensemble model was evaluated based on 10-fold cross-  
233 validation algorithm. The principle of this method meant that the entire datasets were divided into  
234 10 groups with the same capacity randomly. Nine groups were applied to develop the model and the  
235 remained one was used to predict the NO<sub>3</sub><sup>-</sup> level. After ten rounds, every observed NO<sub>3</sub><sup>-</sup>  
236 concentration showed a corresponding predicted value. Some key indices such as determination  
237 coefficient (R<sup>2</sup>), root mean square error (RMSE), and mean absolute prediction error (MAE) were  
238 selected as the key indicators to identify the optimal modelling method.

239 The uncertainty of ensemble model were mainly derived from input ancillary variables. For  
240 instance, both of the satellite data and meteorological data often suffered from some uncertainties.  
241 To quantify the uncertainties derived from meteorological data, the meteorological data at 0.25°

242 across China were validated using ground-measured meteorological data downloaded from the  
243 website of Chinese Meteorology Bureau (<http://data.cma.cn/>). Additionally, NO<sub>2</sub> columns generally  
244 suffered from some uncertainties, whereas the uncertainties of these NO<sub>2</sub> columns cannot be  
245 determined because the data about the ground-level NO<sub>2</sub> columns were not open access. In our study,  
246 we only estimated the missing ratio of NO<sub>2</sub> column, thereby evaluating the uncertainty of NO<sub>3</sub><sup>-</sup>  
247 dataset.

### 248 3.3 Trend analysis

249 The trend analysis of particulate NO<sub>3</sub><sup>-</sup> concentration was performed using the Mann-Kendall  
250 nonparametric test. This method has been widely applied to analyze the historical trends of carbon  
251 fluxes (Tang et al., 2019) and air quality (Kong et al., 2019), which could reflect whether these data  
252 suffered from significant changes at a significance level of 0.05. The detailed calculation process is  
253 summarized in Mann (1945) and Kendall (1975).

## 254 4. Results and discussion

### 255 4.1 Descriptive statistics of observed NO<sub>3</sub><sup>-</sup> concentrations

256 The ensemble model were applied to fit the NO<sub>3</sub><sup>-</sup> estimation model based on 1636 matched  
257 samples across China during 2010-2015. In general, the site-based ground-observed NO<sub>3</sub><sup>-</sup>  
258 concentration over China ranged from 0.3 µg/m<sup>3</sup> µg N m<sup>-3</sup> in Bayinbrook of Xinjiang province to  
259 7.1 µg/m<sup>3</sup> µg N m<sup>-3</sup> in Zhengzhou of Henan province with the mean value of 2.7 ± 1.7 µg/m<sup>3</sup> µg N  
260 m<sup>-3</sup>. The monthly particulate NO<sub>3</sub><sup>-</sup> concentrations displayed the highest and lowest values in North  
261 China Plain (NCP) and Tibetan Plateau, respectively. Besides, the monthly NO<sub>3</sub><sup>-</sup> level exhibited  
262 significantly temporal variation during 2010-2015. The ambient NO<sub>3</sub><sup>-</sup> concentrations in most of sites  
263 displayed the gradual increase during 2010-2014, while they decreased sharply from 2014 to 2015.

264 The spatiotemporal variation of ambient  $\text{NO}_3^-$  concentration over China shared similar characteristic  
265 with  $\text{NO}_2$  column amount and urban land area (Fig. S3). The Pearson correlation analysis revealed  
266 that the monthly particulate  $\text{NO}_3^-$  level showed the significantly positive relationship with  $\text{NO}_2$   
267 column amount ( $r = 0.57$ ,  $p < 0.01$ ) and urban land area ( $r = 0.35$ ,  $p < 0.05$ ) (Fig. S4). However,  $D_{2m}$   
268 showed the remarkably negative correlation with ambient  $\text{NO}_3^-$  concentration ( $r = -0.31$ ,  $p < 0.05$ ).

#### 269 4.2 The validation of new-developed $\text{NO}_3^-$ dataset and comparison with previous products

270 In our study, the ensemble model was applied to develop a monthly particulate  $\text{NO}_3^-$  dataset over  
271 China based on various predictors. Besides, other three individual models were also trained to  
272 compare with their predictive performances. The cross-validation result indicated that the  $R^2$  value  
273 of the new product developed by ensemble decision trees model reached 0.78, significantly higher  
274 than those developed by RF (0.57), GBDT (0.73), and XGBoost (0.45). Nonetheless, both of RMSE  
275 and MAE exhibited the opposite trends. The RMSE value was in the order of XGBoost ( $1.98$   
276  $\mu\text{g}/\text{m}^3 \mu\text{g N m}^{-3}$ ) > RF ( $1.67 \mu\text{g}/\text{m}^3 \mu\text{g N m}^{-3}$ ) > GBDT ( $1.35 \mu\text{g}/\text{m}^3 \mu\text{g N m}^{-3}$ ) > ensemble model ( $1.19$   
277  $\mu\text{g}/\text{m}^3 \mu\text{g N m}^{-3}$ ). The MAE value followed the similar characteristic with the order of XGBoost  
278 ( $1.29 \mu\text{g}/\text{m}^3 \mu\text{g N m}^{-3}$ ) > RF ( $0.99 \mu\text{g}/\text{m}^3 \mu\text{g N m}^{-3}$ ) > GBDT ( $0.95 \mu\text{g}/\text{m}^3 \mu\text{g N m}^{-3}$ ) > ensemble model  
279 ( $0.81 \mu\text{g}/\text{m}^3 \mu\text{g N m}^{-3}$ ). In some previous studies (Xiao et al., 2018), XGBoost often showed the  
280 better performance compared with RF, which seemed to be in contrast to our study. It was assumed  
281 that XGBoost showed the better performance for big-data samples. However, the size of training  
282 samples in our study was relatively less than those in previous studies. Xiao et al. (2018) also  
283 verified that the XGBoost showed the better accuracy than RF in some developed regions such as  
284 East China, while RF showed the better performance than XGBoost in Northwest China because  
285 the monitoring sites in Northwest China was relatively scarce. Wolpert (1992) suggested the

286 combination of various machine-learning models can significantly strengthen the transferability of  
287 models. Chen et al. (2019a) demonstrated that the ensemble model significantly outperformed the  
288 individual machine-learning model because the ensemble model can overcome the weaknesses of  
289 individual model. Besides, we also assessed the annual modelling performance of  $\text{NO}_3^-$  estimation.  
290 Figure S5 shows that the  $R^2$  value of annual  $\text{NO}_3^-$  estimation reached 0.81, slightly higher than  
291 monthly  $\text{NO}_3^-$  prediction (0.78). ~~Furthermore~~However, both of RMSE ( $1.23 \mu\text{g}/\text{m}^3$ ) and  
292 MAE ( $0.85 \mu\text{g}/\text{m}^3$ ) for annual  $\text{NO}_3^-$  estimation were slightly higher than those of monthly  
293  $\text{NO}_3^-$  prediction.

294 The new developed  $\text{NO}_3^-$  dataset showed the markedly temporal discrepancy. The  $R^2$  values of  
295  $\text{NO}_3^-$  estimates during 2011-2015 (0.88, 0.89, 0.83, 0.74, and 0.78) were notably higher than that  
296 during 2010 (0.62) (Table 1 and Fig. 3). The relatively lower  $R^2$  value in 2010 attested to the  
297 dominant role of sampling size on the predictive accuracy for machine-learning models. The training  
298 samples in 2010 (135 samples) were notably less than those in other years due to the lack of  
299 observation data in spring. However, both of RMSE and MAE were not sensitive to the sampling  
300 size. The higher RMSE and MAE focused on the 2010, 2014, and 2015. The higher RMSE and  
301 MAE observed in 2010 might be contributed by the relatively scarce training samples, while the  
302 higher RMSE and MAE likely attained to the higher  $\text{NO}_3^-$  levels during other years. In addition, the  
303 performance of the  $\text{NO}_3^-$  dataset varied greatly at the seasonal scale. The  $R^2$  value was in the order  
304 of summer (0.85) > spring (0.80) = autumn (0.80) > winter (0.75) across China (Table 2). The  
305 seasonal variation of  $\text{NO}_3^-$  concentration was in contrast to the results of fine particle modelled by  
306 previous studies (Li et al., 2020a; Qin et al., 2018). It was supposed that aerosol optical depth (AOD)  
307 was sensitive to the precipitation and relative humidity, and thus showed the worse performance in

308 summer. However, the predictive accuracy of  $\text{NO}_3^-$  estimation based on  $\text{NO}_2$  column amount was  
309 closely linked with the chemical transformation from  $\text{NO}_2$  to  $\text{NO}_3^-$ .

310 The performance of  $\text{NO}_3^-$  dataset also displayed markedly spatial variation. The highest  $R^2$  value  
311 was observed in NCP (0.70), followed by Southwest China (0.60), Southeast China (0.59),  
312 Northwest China (0.55), and the lowest one in Northeast China (0.44) (Table 3). The highest  $R^2$   
313 value occurring in NCP was mainly attributable to the largest training samples ( $> 400$ ) compared  
314 with other regions. Southeast China and Southwest China showed satisfactory cross-validation  $R^2$   
315 values because the valid training samples in both of these regions were higher than 300. Although  
316 both of Northeast China and Northwest China possessed limited training samples ( $< 200$ ), the  
317 predictive performances of these regions showed significant discrepancy. It was assumed that the  
318 sampling sites in Northeast China were very centralized, while the sampling sites in Northwest  
319 China were uniformly distributed across the whole region. Geng et al. (2018) revealed that the  
320 modelling accuracy based on statistical models were significantly affected by the distribution  
321 characteristics of sampling sites. However, both of RMSE and MAE showed different spatial  
322 distributions with the  $R^2$  value and slope of fitting curve. Note that the higher values of RMSE and  
323 MAE were concentrated on Southwest China (2.08 and 1.41  $\mu\text{g}/\text{m}^3 \mu\text{g N m}^{-3}$ ) and Northwest China  
324 (2.06 and 1.38  $\mu\text{g}/\text{m}^3 \mu\text{g N m}^{-3}$ ) rather than NCP (1.74 and 1.06  $\mu\text{g}/\text{m}^3 \mu\text{g N m}^{-3}$ ). There are two  
325 reasons responsible for the result. At first, the predictive performances of Southwest China and  
326 Northwest China were significantly worse than that of NCP, thereby leading to the higher RMSE  
327 and MAE. –Moreover, most of the sampling sites in Southwest China were focused on Sichuan  
328 Basin, which often showed severe  $\text{NO}_3^-$  pollution all the year round. Meanwhile, the annual mean  
329  $\text{NO}_3^-$  concentrations in Yangling and Wuwei reached 4.1 and 4.5  $\mu\text{g}/\text{m}^3 \mu\text{g N m}^{-3}$ , respectively. The

330 higher loadings of  $\text{NO}_3^-$  concentrations for training samples led to the higher RMSE and MAE for  
331 Northwest China.

332 Although the cross-validation result suggested the new developed dataset achieved the better  
333 modelling accuracy, the cross-validation algorithm cannot test the transferability and agreement of  
334 this dataset in the past years. Hence, the unlearned data (annual mean  $\text{NO}_3^-$  concentration in 10 cities)  
335 collected from previous references were employed to validate the transferability of this product. As  
336 shown in Fig. 4 and Table S2, we found that the  $R^2$  value of new-developed  $\text{NO}_3^-$  product and  
337 historical data reached 0.85 (Fig. 4), and the out-of-range  $R^2$  value was even slightly higher than the  
338 cross-validation  $R^2$  value. Moreover, the out-of-bag slope based on these unlearning data reached  
339 0.81, and equaled to the slope of cross-validation database. In addition, the site-based cross-  
340 validation was also applied to validate the transferability of this dataset. The basic principle is that  
341 all of the sites were evenly classified into ten clusters based on the geographical locations.  
342 Afterwards, nine of ten were used to train the model and then test the model based on the remained  
343 one. After ten round, all of the observed values versus estimate values was considered to be the final  
344 result to validate the spatial transferability of this model. As depicted in Fig. S6, the site-based cross-  
345 validation  $R^2$  value reached 0.73, which was slightly lower than the cross-validation  $R^2$  value of the  
346 training model (0.78). The result suggested the new-developed dataset showed excellent  
347 performance in the past decade.

348 Owing to the severe air pollution issue frequently observed in recent years, especially nitrogen-  
349 bearing haze events, many studies have tried to predict the  $\text{NO}_3^-$  concentrations in China. Most of  
350 these studies employed CTMs to simulate the ambient  $\text{NO}_3^-$  concentrations over China. Huang et al.  
351 (2015) employed WRF-CMAQ to estimate the inorganic nitrogen deposition over PRD, and

带格式的: 上标

带格式的: 上标



352 confirmed that the R value only reached 0.54. Afterwards, Han et al. (2017) used RAMS-GMAQ to  
353 predict the dry deposition flux of reactive nitrogen, and significantly underestimated the NO<sub>3</sub><sup>-</sup>  
354 concentration in the atmosphere. Very recently, Geng et al. (2019) used CMAQ to estimate the NO<sub>3</sub><sup>-</sup>  
355 concentrations over East China, and the predictive performance (R = 0.53) showed the similar result  
356 to Huang et al. (2015). Apart from these CTMs, the statistical models also has been applied to  
357 estimate the ambient NO<sub>3</sub><sup>-</sup> concentration over China. Unfortunately, the predictive accuracy was not  
358 good based on traditional statistical models (e.g., linear regression) (R = 0.47) (Jia et al., 2016). In  
359 terms of model performance, the developed NO<sub>3</sub><sup>-</sup> product in our study was much better than those  
360 developed by pioneering studies. Furthermore, this product showed many extra advantages than  
361 those obtained by CTMs especially for the hindeast estimates of air pollutants. For instance, CTMs  
362 generally required continuous emission inventory data, which were often not available and showed  
363 high uncertainties. Moreover, CTMs generally needed substantial computing time and big-data  
364 input data to ensure the reliable predictive accuracy. Thus, the NO<sub>3</sub><sup>-</sup> product retrieved by CTMs  
365 often lacks of long-term dataset (> 10 yr), and our study fills the gaps of previous studies.

#### 366 4.3 Spatial pattern of new-developed NO<sub>3</sub><sup>-</sup> dataset

367 The monthly NO<sub>3</sub><sup>-</sup> concentration displayed the similar distribution characteristic with PM<sub>2.5</sub> and  
368 PM<sub>1</sub> (Wei et al., 2019). Overall, the NO<sub>3</sub><sup>-</sup> concentration in East China was much higher than that in  
369 West China. The higher NO<sub>3</sub><sup>-</sup> concentration was concentrated on NCP ( $3.55 \pm 1.25 \mu\text{g}/\text{m}^3 \mu\text{g N m}^{-3}$ )  
370 <sup>3</sup>), followed by Yangtze River Delta (YRD ( $2.56 \pm 1.12 \mu\text{g}/\text{m}^3 \mu\text{g N m}^{-3}$ )), Pearl River Delta (PRD  
371 ( $1.68 \pm 0.81 \mu\text{g}/\text{m}^3 \mu\text{g N m}^{-3}$ )), Sichuan Basin ( $1.53 \pm 0.63 \mu\text{g}/\text{m}^3 \mu\text{g N m}^{-3}$ ), and the lowest one  
372 observed in Tibetan Plateau ( $0.42 \pm 0.25 \mu\text{g}/\text{m}^3 \mu\text{g N m}^{-3}$ ) (Fig. 5). Most provinces over NCP such  
373 as Beijing, Hebei, Henan, and Shandong suffered from severe NO<sub>3</sub><sup>-</sup> pollution due to dense human

374 activities and strong industry foundation (Li et al., 2017) (Fig. S7), which released a large amount  
375 of N-bearing gaseous pollutants to the atmosphere especially in winter. In BTH ( $2.97 \pm 1.97$   
376  $\mu\text{g}/\text{m}^3$   $\mu\text{g N m}^{-3}$ ), Wang et al. (2016) verified that these fresh  $\text{NO}_x$  emitted from power plants or  
377 cement industries could be transformed into the nitrate in the particulate phase by the aid of low air  
378 temperature. In YRD and PRD, the combustion of fossil fuels and traffic emissions were considered  
379 to be the major source of  $\text{NO}_x$  emission, which favored to the formation of nitrate event through the  
380 gas-particle conversion processes (Fu et al., 2017; Kong et al., 2020; Ming et al., 2017). Apart from  
381 the contributions of smelting industries, the poor topographical or meteorological conditions were  
382 also responsible for the severe  $\text{NO}_3^-$  pollution in Sichuan Basin (Tian et al., 2017; Wang et al., 2017).  
383 Tibetan Plateau generally showed the clean air quality due to the unique landform and scarce  
384 industrial activity (Yang et al., 2018). In addition, it was interesting to note that the Altai region and  
385 Taklimakan desert in Xinjiang autonomous region also showed some  $\text{NO}_3^-$  hotspots, though these  
386 regions were often believed to be the remote region. It was assumed that the many petrochemical  
387 industries (e.g., Karamai oil field) were located in the Altai region (Liu et al., 2018). Besides, Qi et  
388 al. (2018) verified that the resuspension of soil dust might trigger the accumulation of  $\text{NO}_3^-$   
389 concentration in the aerosol.

#### 390 4.4 Long-term trend of ambient $\text{NO}_3^-$ across China

391 The temporal variation of  $\text{NO}_3^-$  levels from 2005 to 2015 over China has been clarified in Fig.  
392 6, Fig. 7 and Table S2S3. Overall, the ambient  $\text{NO}_3^-$  concentration in China showed the significant  
393 increasing trend of  $0.10 \mu\text{g}/\text{m}^3$   $\mu\text{g N m}^{-3}/\text{year}$  during 2005-2014, while it decreased sharply from  
394 2014 to 2015 by ~~the speed of~~  $-0.40 \mu\text{g}/\text{m}^3$   $\mu\text{g N m}^{-3}/\text{year}$ . Overall, more than 90% areas of Mainland  
395 China showed consistent temporal variation with the gradual increase from 2005 to 2013/2014, and

396 then rapid decrease from 2013/2014 to 2015. However, the decreasing/increasing speed displayed  
397 significantly spatial difference in some major regions of China. For instance, the ambient  $\text{NO}_3^-$  level  
398 in BTH showed the remarkable increase during 2005-2013 by ~~the speed of~~  $0.20 \mu\text{g}/\text{m}^3 \mu\text{g N m}^{-3}/\text{year}$ .  
399 Afterwards, the  $\text{NO}_3^-$  level decreased rapidly from 2013 to 2015 at a ~~speed-rate~~ of  $-0.58 \mu\text{g}/\text{m}^3 \mu\text{g N}$   
400  $\text{m}^{-3}/\text{year}$ . The  $\text{NO}_3^-$  concentrations in YRD ( $0.11 \mu\text{g}/\text{m}^3 \mu\text{g N m}^{-3}/\text{year}$ ) and PRD ( $0.05 \mu\text{g}/\text{m}^3 \mu\text{g N}$   
401  $\text{m}^{-3}/\text{year}$ ) both showed the slight increases during 2005-2013, though the statistical test revealed the  
402 increases were significant ( $p < 0.05$ ). However, the  $\text{NO}_3^-$  concentrations in YRD and PRD showed  
403 the dramatic decreases with  $-0.48$  and  $-0.36 \mu\text{g}/\text{m}^3 \mu\text{g N m}^{-3}/\text{year}$  during 2013-2015, respectively. As  
404 seen from 2005 to 2015, the  $\text{NO}_3^-$  concentration in BTH displayed the slight increase during this  
405 period. Nevertheless, the  $\text{NO}_3^-$  levels in YRD and PRD both displayed the slow decreases by ~~the~~  
406 ~~speed of~~  $-0.01$  and  $-0.03 \mu\text{g}/\text{m}^3 \mu\text{g N m}^{-3}/\text{year}$ , respectively.

407 Furthermore, the different provinces displayed disparate temporal variations especially during  
408 11th five year plan (2005-2010). 31 provinces (municipalities/autonomous region) of China can be  
409 classified into three clusters based on the temporal trends of  $\text{NO}_3^-$  concentrations during 11th five  
410 year plan. The first cluster featured the gradual increase of  $\text{NO}_3^-$  concentration during this period,  
411 which consisted of three provinces in Northeast China (e.g., Heilongjiang) and central provinces in  
412 South China (e.g., Jiangxi, Anhui) (Table S2S3). The second cluster represented the provinces with  
413 the stable increases of  $\text{NO}_3^-$  during 2005-2007 and slight decreases during 2007-2010. Some  
414 provinces of NCP (e.g., Beijing, Hebei, Henan) and Northwest China (e.g., Gansu, Inner Mongolia,  
415 Ningxia) fell into the second cluster. The last cluster featured the opposite temporal trend to the  
416 second cluster during 2005-2010, which included many southern provinces such as Fujian,  
417 Guangdong, Zhejiang, and Guangxi. Although the central government proposed the emission

418 reduction goal in 2006, the ambient  $\text{NO}_3^-$  concentrations in most provinces did not display  
419 pronounced decreases, which was totally different from the decrease of  $\text{PM}_{2.5}$  since 2007 (Xue et  
420 al., 2019). Especially in the provinces of Northeast China (e.g., Liaoning), the ambient  $\text{NO}_3^-$   
421 concentrations in these provinces still showed the rapid increases after the proposal of emission  
422 control measures. It was assumed that these provinces generally possessed a large amount of energy-  
423 intensive industries and coal-fired power plants (Zhang et al., 2018). Moreover, the result might be  
424 associated with the fact that the emission reduction measures focused on the reduction of  $\text{SO}_2$   
425 emission rather than  $\text{NO}_x$  emission (Kanada et al., 2013). Schreifels et al. (2012) revealed that major  
426 control measures during this period included shutting down inefficient industries, increasing the  
427 pollution levy for excessive  $\text{SO}_2$  emissions, and implementing energy conservation projects.  
428 Therefore, the total  $\text{SO}_2$  emission in 2010 decreased by more than 14% compared with the emission  
429 in 1995 and the ambient  $\text{SO}_2$  concentrations in many provinces since 2005 displayed significant  
430 decreases compared with those in 1990s (Li et al., 2020b; Lu et al., 2013; Zhou et al., 2015).  
431 Nonetheless, the  $\text{NO}_x$  emission in China did not display significant decrease during this period  
432 (Duncan et al., 2016; Granier et al., 2017), and thus the ambient  $\text{NO}_3^-$  in many provinces still kept  
433 the higher concentrations. It should be noted that the  $\text{NO}_3^-$  concentrations in some provinces of NCP  
434 exactly exhibited the slow decreases after 2007. It was supposed that the energy structure adjustment  
435 and elimination of backward production capacity promoted the small decrease of  $\text{NO}_3^-$   
436 concentrations (Ma et al., 2019). Unfortunately, the slight decreases were quickly offset by the rapid  
437 increase of energy consumption. Zhang et al. (2018) demonstrated that the industry added values  
438 and private car number in BTH have been increasing by 189.4% and 279.6% during 2005-2010,  
439 respectively. In addition, the decrease of  $\text{SO}_2$  emission rather than  $\text{NO}_x$  emission can further lead to

带格式的: 下标

带格式的: 下标

440 NO<sub>3</sub><sup>-</sup> increase because of decreased aerosol acidity, which was dictated by SO<sub>4</sub><sup>2-</sup> in particulate matter  
441 (Xie et al., 2020; Vasilakos et al., 2018).

442 Since 2010, the central government began to implement severe limitations in PM<sub>2.5</sub>, NO<sub>x</sub>, and  
443 soot emissions, and thus the total NO<sub>x</sub> emission during 11th five year plan (2011-2015) showed  
444 slow decrease (10%) across China (Ma et al., 2019). However, the NO<sub>3</sub><sup>-</sup> concentrations across China  
445 did not show rapid response to the emission control measures. For instance, the NO<sub>3</sub><sup>-</sup> concentrations  
446 in most provinces of China still showed rapid increases during 2010-2013 (2014) (Fig. 7 and Fig.  
447 8). The result suggested that the control measures about the NO<sub>x</sub> emissions from vehicles and ships  
448 might be not very effective. Until 2013, the central government issued Action Plan for Air Pollution  
449 Prevention and Control (APPC-AP) in order to enhance the air pollution prevention measures (Li et  
450 al., 2017; Li et al., 2019). Many powerful economic and policy means including pricing (tax) policy  
451 and optimization of industrial layout caused the rapid decreases of NO<sub>3</sub><sup>-</sup> concentrations after 2013  
452 in many provinces (e.g., Beijing, Hebei, Zhejiang). Wang et al. (2019b) also verified that the NO<sub>3</sub><sup>-</sup>  
453 level in PM<sub>2.5</sub> over BTH has decreased by 20% during 2013-2015, which was in accordance with  
454 the finding of our study. In addition to the impact of emission reduction, the rapid decrease of NO<sub>3</sub><sup>-</sup>  
455 concentration over China after 2013 might be linked with the beneficial meteorological factors  
456 because Chen et al. (2019c) has demonstrated that favorable meteorological conditions led to about  
457 20% of the PM<sub>2.5</sub> decrease in BTH during 2013-2015. However, the decreasing trend of NO<sub>3</sub><sup>-</sup>  
458 concentration during 2014-2015 in PRD (-0.36  $\mu\text{g}/\text{m}^3 \mu\text{g N m}^{-3}/\text{year}$ ) was significantly slower than  
459 that in BTH (-0.58  $\mu\text{g}/\text{m}^3 \mu\text{g N m}^{-3}/\text{year}$ ) and YRD (-0.48  $\mu\text{g}/\text{m}^3 \mu\text{g N m}^{-3}/\text{year}$ ) (Table 4). Wang et  
460 al. (2019b) found that the ambient NO<sub>3</sub><sup>-</sup> concentration in a background site of PRD even showed an  
461 upward trend during 2014-2016. Thus, it was necessary to strengthen the control of nitrogen oxide

带格式的: 下标

带格式的: 上标

带格式的: 下标

带格式的: 上标

462 emissions.

463 In general, the ambient  $\text{NO}_3^-$  concentration varied greatly at the seasonal scale (Fig. 9). China  
464 undergone the most serious  $\text{NO}_3^-$  pollution in winter ( $1.57 \pm 0.63 \mu\text{g}/\text{m}^3 \mu\text{g N m}^{-3}$ ), followed by  
465 autumn ( $1.09 \pm 0.52 \mu\text{g}/\text{m}^3 \mu\text{g N m}^{-3}$ ), spring ( $0.78 \pm 0.50 \mu\text{g}/\text{m}^3 \mu\text{g N m}^{-3}$ ), and the lowest one in  
466 summer ( $0.63 \pm 0.40 \mu\text{g}/\text{m}^3 \mu\text{g N m}^{-3}$ ) (Table S3S4). The higher  $\text{NO}_3^-$  concentration observed in  
467 winter might be contributed by the dense coal combustion in North China and unfavorable  
468 meteorological conditions (Itahashi et al., 2017; Quan et al., 2014; Wang et al., 2019d). The lightest  
469  $\text{NO}_3^-$  pollution in summer was attributable to the abundant precipitation, which promoted the  
470 diffusion and removal of pollutants and reduced ambient  $\text{NO}_3^-$  level (Hu et al., 2005). The ratio of  
471  $\text{NO}_3^-$  concentration in winter ( $\text{NO}_3^-_{\text{winter}}$ ) and that in summer ( $\text{NO}_3^-_{\text{summer}}$ ) varied greatly at the spatial  
472 scale. The  $\text{NO}_3^-_{\text{winter}}/\text{NO}_3^-_{\text{summer}}$  in some provinces (municipalities) including Tianjin (2.11), Hebei  
473 (2.25), and Henan (2.84) displayed the higher values compared with other provinces. The higher  
474  $\text{NO}_3^-_{\text{winter}}/\text{NO}_3^-_{\text{summer}}$  in NCP might be affected by the fossil fuel combustion for domestic heating,  
475 while some southern provinces did not need domestic heating in winter. In contrast, the ratio of  $\text{NO}_3^-_{\text{winter}}/\text{NO}_3^-_{\text{summer}}$   
476 exhibited the lower values in some western provinces such as Tibet and Qinghai. It  
477 might be probably associated with the less aerosol emission from anthropogenic source and the  
478 higher wind speed (Wei et al., 2019).

#### 479 4.5 Uncertainty analysis of $\text{NO}_3^-$ estimation

480 The ensemble model of three machine-learning algorithms captured the better accuracy in  
481 predicting the  $\text{NO}_3^-$  level from OMI data. Nonetheless, the ensemble model still showed some  
482 improvement space in terms of the  $R^2$  value. At first, meteorological data collected from reanalysis  
483 in ECMWF website generally showed high uncertainty, which inevitably increased the error of  $\text{NO}_3^-$

484 estimation. In our study, we validated the gridded  $T_{2m}$  and  $T_p$  datasets against the ground-observed  
485 datasets and found that the  $R^2$  values of  $T_{2m}$  and  $T_p$  reached 0.98 and 0.83 (Table S4S5), respectively.  
486 The result suggested that  $T_{2m}$  showed the lower uncertainty, while  $T_p$  displayed relatively higher  
487 uncertainty. Except  $T_{2m}$  and  $T_p$ , the ground-level datasets for other meteorological factors were not  
488 open access, and thus we cannot assess their uncertainties. Thus, we only reviewed some references  
489 and evaluated their uncertainties. For instance, Guo et al. 2019 found that the reanalysis BLH data  
490 also exhibited large uncertainties because few sounding data were assimilated. These uncertainties  
491 derived from predictors could be passed to the ensemble model, and thus increased the uncertainties  
492 of ambient  $NO_3^-$  estimates.

493 The second reason was closely linked to the missing  $NO_2$  column amount across China. The  
494  $NO_2$  column amount retrieval showed many nonrandom biases especially for the arid or semi-arid  
495 area with high surface reflectance. The missing  $NO_2$  column amounts over China were not filled in  
496 our study due to the increased uncertainty of filling  $NO_2$  column. Moreover, it should be noted that  
497 the monthly  $NO_2$  column amounts were averaged based on the daily one, and the missing ratio of  
498 daily  $NO_2$  columns during 2005-2015 reached 57.64%, the higher missing ratio might increase the  
499 uncertainty of  $NO_3^-$  simulation.

500 Lastly, the developed ensemble model did not integrate the direct spatiotemporal weight  
501 indicators (e.g., the distance of observed sites and contiguous grids) though many predictors (e.g.,  
502 month of year) reflecting spatiotemporal autocorrelation were input into the original model as the  
503 key predictors. Furthermore, the developed model was the ensemble one of three original models,  
504 which ignored the spatiotemporal autocorrelation of estimation residues from first-stage model. In  
505 the future work, the ensemble model could be combined with a space-time model to further enhance

506 the modelling performance.

## 507 **5. Data availability**

508 The monthly  $\text{NO}_3^-$  datasets at  $0.25^\circ$  resolution across China during 2005-2015 are available at  
509 <https://doi.org/10.5281/zenodo.3988307> (Li et al., 2020), which can be downloaded in xlsx format.

510 The missing values are shown in NaN.

## 511 **6. Conclusions and implications**

512 In this study, RF, GBDT, and XGBoost algorithms were combined to establish a high-resolution  
513 ( $0.25^\circ$ )  $\text{NO}_3^-$  dataset over China during 2005-2015 on the basis of multi-source predictors. The  $\text{NO}_3^-$   
514 product showed high cross-validation  $R^2$  value (0.78), but low RMSE ( $1.19 \mu\text{g}/\text{m}^3 \mu\text{g N m}^{-3}$ ) and  
515 MAE ( $0.81 \mu\text{g}/\text{m}^3 \mu\text{g N m}^{-3}$ ). The  $\text{NO}_3^-$  dataset showed the markedly spatiotemporal discrepancy.  
516 The  $R^2$  value was in the order of summer (0.85) > spring (0.80) = autumn (0.80) > winter (0.75)  
517 across China, and the  $R^2$  showed the highest value in NCP. In addition, the dataset exhibited  
518 excellent transferability ( $R^2 = 0.85$ , RMSE =  $0.74 \mu\text{g}/\text{m}^3 \mu\text{g N m}^{-3}$ , and MAE =  $0.55 \mu\text{g}/\text{m}^3 \mu\text{g N m}^{-3}$ )  
519 on the basis of the unlearning observed data in ten sites.

520 The new-developed  $\text{NO}_3^-$  dataset showed remarkably predictive accuracy compared with  
521 previous products developed by CTMs and linear regression model. The result might be linked to  
522 two key reasons. First of all, the new product assimilated high-resolution  $\text{NO}_2$  column amount  
523 instead of the  $\text{NO}_x$  emission inventory used by CTMs. The imperfect knowledge about the chemical  
524 modules with regard of the  $\text{NO}_3^-$  formation and the inaccurate emission inventory decreased the  
525 predictive performance of CTMs. In contrast, the new product was obtained using ensemble  
526 machine-learning model, which did not need to consider the photochemical or aqueous process from  
527 gaseous  $\text{NO}_2$  to particulate  $\text{NO}_3^-$ . Compared with the  $\text{NO}_3^-$  product estimated by linear regression



528 model ( $R^2 = 0.21$ ), the new product significantly elevated the modelling performance of  $\text{NO}_3^-$   
529 concentration. It was supposed that the ensemble model for the development of the new  $\text{NO}_3^-$  dataset  
530 did not predefine the potential relationships between explanatory variables and  $\text{NO}_3^-$  level as the  
531 multiple regression model, which must assume the linear linkage between dependent variable and  
532 predictors before model establishment.

533 On the basis of the such dataset, the spatiotemporal variation of  $\text{NO}_3^-$  concentration over China  
534 during 2005-2015 were clarified. The annual mean  $\text{NO}_3^-$  concentration followed the order of NCP  
535 ( $3.55 \pm 1.25 \mu\text{g}/\text{m}^3 \mu\text{g N m}^{-3}$ ) > YRD ( $2.56 \pm 1.12 \mu\text{g}/\text{m}^3 \mu\text{g N m}^{-3}$ ) > PRD ( $1.68 \pm 0.81 \mu\text{g}/\text{m}^3 \mu\text{g N}$   
536  $\text{m}^{-3}$ ) > Sichuan Basin ( $1.53 \pm 0.63 \mu\text{g}/\text{m}^3 \mu\text{g N m}^{-3}$ ) > Tibetan Plateau ( $0.42 \pm 0.25 \mu\text{g}/\text{m}^3 \mu\text{g N m}^{-3}$ ).

537 The higher  $\text{NO}_3^-$  concentrations in NCP, YRD, and PRD were mainly contributed by the intensive  
538 industrial and traffic emissions. Sichuan Basin suffered serious  $\text{NO}_3^-$  pollution due to the high  
539 loadings of aerosols and unfavorable terrain condition. Tibetan Plateau shared with the lightest  $\text{NO}_3^-$   
540 pollution because of the scarce anthropogenic emissions and favorable meteorological factors.

541 Additionally, we also found that the ambient  $\text{NO}_3^-$  concentration showed significant increasing trend  
542 of  $0.10 \mu\text{g}/\text{m}^3 \mu\text{g N m}^{-3}/\text{year}$  during 2005-2014, while it decreased sharply from 2014 to 2015 at a  
543 rate of  $-0.40 \mu\text{g}/\text{m}^3 \mu\text{g N m}^{-3}/\text{year}$ . The ambient  $\text{NO}_3^-$  levels in BTH, YRD, and PRD displayed slight  
544 increases at the rate of 0.20, 0.11, and  $0.05 \mu\text{g}/\text{m}^3 \mu\text{g N m}^{-3}/\text{year}$  during 2013-2015, respectively.

545 Afterwards, the  $\text{NO}_3^-$  concentrations decreased sharply at the speed of -0.58, -0.48, and -0.36  
546  $\mu\text{g}/\text{m}^3 \mu\text{g N m}^{-3}/\text{year}$ . Although National Economic and Social Development of China has issued the  
547 emission reduction goal in 2006, the  $\text{NO}_3^-$  concentrations in most provinces did not show the  
548 significant decreases during 2005-2010. It might be contributed by the increase of energy  
549 consumption and non-targeted emission control measures. Since 2010, the government began to

550 decrease the  $\text{NO}_x$  emission over China, whereas the  $\text{NO}_3^-$  concentrations in many provinces still  
551 showed slight increases during 2010-2014 because the benefits of control measures for  $\text{NO}_x$   
552 emission could be neutralized by elevated energy consumption along with the rapid economic  
553 development. Since 2014, Chinese government issued APPC-AP and further enhanced the emission  
554 control measures, and triggered the dramatic decrease of  $\text{NO}_3^-$  concentration over China. Apart from  
555 the effect of emission reduction, the favorable meteorological conditions might lead to the rapid  
556 decrease of  $\text{NO}_3^-$  level over China during 2014-2015. Compared with the powerful emission control  
557 measures, meteorological factors only contributed a small portion of  $\text{NO}_3^-$  reduction in China.  
558 Besides, the decrease speed of  $\text{NO}_3^-$  level in China also displayed pronounced spatial heterogeneity  
559 and some background region even featured the upward of air pollutant in recent years. Therefore, it  
560 is still imperative to strengthen the emission reduction measures.

561 It must be acknowledged that our study still suffers from some limitations. First of all, the  $\text{NO}_3^-$   
562 dataset was developed by machine-learning models, which lacked of the chemical module  
563 concerning about the transformation pathway from  $\text{NO}_2$  to  $\text{NO}_3^-$ , and might underestimate the  
564 ambient  $\text{NO}_3^-$  concentration across China. In the future work, the output results of CTMs including  
565 conversion ratio from  $\text{NO}_2$  to  $\text{NO}_3^-$ , dry/wet deposition flux of  $\text{NO}_2$  and  $\text{NO}_3^-$  in the atmosphere  
566 should be incorporated into the machine-learning model to develop next-generation  $\text{NO}_3^-$  product.  
567 Second, the low time-resolution (monthly) observation data hindered the daily estimation of  $\text{NO}_3^-$   
568 concentration. The daily  $\text{NO}_3^-$  datasets are warranted in the future because it could be used to assess  
569 the potential impact on human health. Besides, the ultrahigh-resolution satellite (TROPOMI) can  
570 allow continuation and enhancement of the spatiotemporal  $\text{NO}_3^-$  estimation though the OMI product  
571 could capture enough spatial variations across China.

572 **Acknowledgements**

573 This work was funded by Chinese Postdoctoral Science Foundation (2020M680589) and National  
574 Natural Science Foundation of China (Nos. 21777025).

575 **Author contributions**

576 Rui Li, Lulu Cui, and Hongbo Fu conceived and designed the study. Rui Li, Lulu Cui, Yilong Zhao,  
577 Wenhui Zhou collected and processed the data. Rui Li wrote this paper with contributions from all  
578 of the coauthors.

579 **References**

- 580 Breiman, L.: Random forests. *Machine learning* 45, 5-32, 2001.
- 581 Chen, H., Li, D., Gurmesa, G.A., Yu, G., Li, L., Zhang, W., Fang, H., Mo, J.: Effects of nitrogen  
582 deposition on carbon cycle in terrestrial ecosystems of China: A meta-analysis. *Environ. Pollut.* 206,  
583 352-360, <https://doi.org/10.1016/j.envpol.2015.07.033>, 2015.
- 584 Chen, J., Yin, J., Zang, L., Zhang, T., Zhao, M.: Stacking machine learning model for estimating hourly  
585 PM<sub>2.5</sub> in China based on Himawari-8 aerosol optical depth data. *Sci. Total Environ.* 697, 134021,  
586 <https://doi.org/10.1016/j.scitotenv.2019.134021>, 2019a.
- 587 Chen, Z.Y., Zhang, R., Zhang, T.H., Ou, C.Q., Guo, Y.: A kriging-calibrated machine learning method  
588 for estimating daily ground-level NO<sub>2</sub> in mainland China. *Sci. Total Environ.* 690, 556-564,  
589 <https://doi.org/10.1016/j.scitotenv.2019.06.349>, 2019b.
- 590 Chen, Z., Chen, D., Kwan, M., Chen, B., Cheng, N., Gao, B., Zhuang, Y., Li, R., and Xu, B.: The control  
591 of anthropogenic emissions contributed to 80 % of the decrease in PM<sub>2.5</sub> concentrations in Beijing  
592 from 2013 to 2017, *Atmos. Chem. Phys. Discuss.*, <https://doi.org/10.5194/acp-2018-1112>, 2019c.
- 593 Compton, J.E., Harrison, J.A., Dennis, R.L., Greaver, T.L., Hill, B.H., Jordan, S.J., Walker, H., Campbell,  
594 H.V.: Ecosystem services altered by human changes in the nitrogen cycle: a new perspective for US  
595 decision making. *Ecology letters* 14, 804-815, <https://doi.org/10.1111/j.1461-0248.2011.01631.x>,  
596 2011.
- 597 Cui, S., Shi, Y., Malik, A., Lenzen, M., Gao, B., Huang, W.: A hybrid method for quantifying China's  
598 nitrogen footprint during urbanisation from 1990 to 2009. *Environ. Interna.* 97, 137-145,  
599 <https://doi.org/10.1016/j.envint.2016.08.012>, 2016.
- 600 Du, E., de Vries, W., Galloway, J.N., Hu, X., Fang, J.: Changes in wet nitrogen deposition in the United

601 States between 1985 and 2012. *Environ. Res. Lett.* 9, 095004, 2014.

602 Duncan, B.N., Lamsal, L.N., Thompson, A.M., Yoshida, Y., Lu, Z., Streets, D.G., Hurwitz, M.M.,  
603 Pickering, K.E.: A space-based, high-resolution view of notable changes in urban NO<sub>x</sub> pollution  
604 around the world (2005–2014). *J. Geophys. Res.* 121, 976-996, <https://doi.org/10.1002/2015JD024121>,  
605 2016.

606 Erisman, J.W., Galloway, J.N., Seitzinger, S., Bleeker, A., Dise, N.B., Petrescu, A.R., Leach, A.M., de  
607 Vries, W.: Consequences of human modification of the global nitrogen cycle. *Philosophical*  
608 *Transactions of the Royal Society B: Biological Sciences* 368, 20130116,  
609 <https://doi.org/10.1098/rstb.2013.0116>, 2013.

610 Fu, H., Chen, J.: Formation, features and controlling strategies of severe haze-fog pollutions in China.  
611 *Sci. Total Environ.* 578, 121-138, <https://doi.org/10.1016/j.scitotenv.2016.10.201>, 2017.

612 Fu, X., Wang, S., Xing, J., Zhang, X., Wang, T., Hao, J.: Increasing ammonia concentrations reduce the  
613 effectiveness of particle pollution control achieved via SO<sub>2</sub> and NO<sub>x</sub> emissions reduction in east China.  
614 *Environ. Sci. Tech. Lett.* 4, 221-227, <https://doi.org/10.1021/acs.estlett.7b00143>, 2017.

615 Georgoulias, A. K., van der A, R. J., Stammes, P., Boersma, K. F., and Eskes, H. J.: Trends and trend  
616 reversal detection in 2 decades of tropospheric NO<sub>2</sub> satellite observations, *Atmos. Chem. Phys.*, 6269-  
617 6294, <https://doi.org/10.5194/acp-19-6269-2019>, 2019.

618 Granier, C., Granier, L., Sindelarova, K., Liousse, C., Darras, S., Bouarar, I., van der Gon, H.D., Frost,  
619 G.J., Janssens-Maenhout, G., Crippa, M.: Trends in anthropogenic emissions from 1960 to 2015. *Hal.*  
620 *Archives*, 2017.

621 Guo, J., Su, T., Chen, D., Wang, J., Li, Z., Lv, Y., Guo, X., Liu, H., Cribb, M., Zhai, P.: Declining  
622 Summertime Local-Scale Precipitation Frequency Over China and the United States, 1981–2012. *The*

623 Disparate Roles of Aerosols. *Geophys. Res. Lett.* 46, 13281-13289,  
624 <https://doi.org/10.1029/2019GL085442>, 2019.

625 Han, X., Zhang, M., Skorokhod, A., Kou, X.: Modeling dry deposition of reactive nitrogen in China with  
626 RAMS-CMAQ. *Atmos. Environ.* 166, 47-61, <https://doi.org/10.1016/j.atmosenv.2017.07.015>, 2017.

627 Hu, M., Zhang, J., Wu, Z.: Chemical compositions of precipitation and scavenging of particles in Beijing.  
628 *Sci. China B* 48, 265-272, *Science in China Series B: Chemistry*, 2005.

629 Huang, Z., Wang, S., Zheng, J., Yuan, Z., Ye, S., Kang, D.: Modeling inorganic nitrogen deposition in  
630 Guangdong province, China. *Atmos. Environ.* 109, 147-160,  
631 <https://doi.org/10.1016/j.atmosenv.2015.03.014>, 2015.

632 Itahashi, S., Uno, I., Osada, K., Kamiguchi, Y., Yamamoto, S., Tamura, K., Wang, Z., Kurosaki, Y.,  
633 Kanaya, Y.: Nitrate transboundary heavy pollution over East Asia in winter. *Atmos. Chem. Phys.* 17,  
634 3823-3843, 2017.

635 Jia, Y., Yu, G., Gao, Y., He, N., Wang, Q., Jiao, C., Zuo, Y.: Global inorganic nitrogen dry deposition  
636 inferred from ground-and space-based measurements. *Sci. Rep.* 6, 19810, [10.1038/srep19810](https://doi.org/10.1038/srep19810), 2016.

637 Kanada, M., Dong, L., Fujita, T., Fujii, M., Inoue, T., Hirano, Y., Togawa, T., Geng, Y.: Regional disparity  
638 and cost-effective SO<sub>2</sub> pollution control in China: A case study in 5 mega-cities. *Energ. Policy* 61,  
639 1322-1331, <https://doi.org/10.1016/j.enpol.2013.05.105>, 2013.

640 Kendall, M.G.: *Rank Correlation methods*[M] Charles Griffin, London, 1975.

641 Kong, L., Hu, M., Tan, Q., Feng, M., Qu, Y., An, J., Zhang, Y., Liu, X., Cheng, N.: Aerosol optical  
642 properties under different pollution levels in the Pearl River Delta (PRD) region of China. *J. Environ.*  
643 *Sci.* 87, 49-59, <https://doi.org/10.1016/j.jes.2019.02.019>, 2020.

644 Kong, L., Tang, X., Zhu, J., Wang, Z.F., Li, J.J., Wu, H.J., Carmichael, G.R.: A Six-year long (2013–

645 2018) High-resolution Air Quality Reanalysis Dataset over China base on the assimilation of surface  
646 observations from CNEMC. Earth Sys. Sci. Data, <https://doi.org/10.5194/essd-2020-100>, 2019.

647 Li, R., Cui, L., Hongbo, F., Li, J., Zhao, Y., Chen, J.: Satellite-based estimation of full-coverage ozone  
648 ( $O_3$ ) concentration and health effect assessment across Hainan Island. J. Cleaner Prod. 244, 118773,  
649 <https://doi.org/10.1016/j.jclepro.2019.118773>, 2020a.

650 Li, R., Cui, L., Li, J., Zhao, A., Fu, H., Wu, Y., Zhang, L., Kong, L., Chen, J.: Spatial and temporal  
651 variation of particulate matter and gaseous pollutants in China during 2014-2016. Atmos. Environ.  
652 161, 235-246, <https://doi.org/10.1016/j.atmosenv.2017.05.008>, 2017.

653 Li, R., Cui, L., Liang, J., Zhao, Y., Zhang, Z., Fu, H.: Estimating historical  $SO_2$  level across the whole  
654 China during 1973–2014 using random forest model. Chemosphere, 125839,  
655 <https://doi.org/10.1016/j.chemosphere.2020.125839>, 2020b.

656 Li, R., Wang, Z., Cui, L., Fu, H., Zhang, L., Kong, L., Chen, W., Chen, J.: Air pollution characteristics  
657 in China during 2015–2016: Spatiotemporal variations and key meteorological factors. Sci. Total  
658 Environ. 648, 902-915, <https://doi.org/10.1016/j.scitotenv.2018.08.181>, 2019.

659 Li, R., Cui, L.L., Zhao, Y.L., Zhou, W.H., Fu, H.B.: Long-term trends of ambient nitrate ( $NO_3^-$ )  
660 concentrations across China based on ensemble machine-learning models,  
661 <https://doi.org/10.5281/zenodo.3988307>, 2020c.

662 Liu, L., Zhang, X., Xu, W., Liu, X., Li, Y., Lu, X., Zhang, Y., Zhang, W.: Temporal characteristics of  
663 atmospheric ammonia and nitrogen dioxide over China based on emission data, satellite observations  
664 and atmospheric transport modeling since 1980. Atmos. Chem. Phys. 17, 9365-9378, 2017a.

665 Liu, X., Duan, L., Mo, J., Du, E., Shen, J., Lu, X., Zhang, Y., Zhou, X., He, C., Zhang, F.: Nitrogen  
666 deposition and its ecological impact in China: an overview. Environ. Pollut. 159, 2251-2264,

667 <https://doi.org/10.1016/j.envpol.2010.08.002>, 2011.

668 Liu, X., Xu, W., Duan, L., Du, E., Pan, Y., Lu, X., Zhang, L., Wu, Z., Wang, X., Zhang, Y.: Atmospheric  
669 nitrogen emission, deposition, and air quality impacts in China: An overview. *Curr. Pollut. Rep.* 3, 65-  
670 77, 2017b.

671 Liu, Z., Gao, W., Yu, Y., Hu, B., Xin, J., Sun, Y., Wang, L., Wang, G., Bi, X., Zhang, G.: Characteristics  
672 of PM<sub>2.5</sub> mass concentrations and chemical species in urban and background areas of China: emerging  
673 results from the CARE-China network. *Atmos. Chem. Phys.* 18, 1-34, [https://www.atmos-chem-](https://www.atmos-chem-phys.net/18/8849/2018/acp-18-8849-2018-discussion.html)  
674 [phys.net/18/8849/2018/acp-18-8849-2018-discussion.html](https://www.atmos-chem-phys.net/18/8849/2018/acp-18-8849-2018-discussion.html), 2018.

675 Lu, Z., Streets, D.G., de Foy, B., Krotkov, N.A.: Ozone Monitoring Instrument observations of  
676 interannual increases in SO<sub>2</sub> emissions from Indian coal-fired power plants during 2005-2012. *Environ.*  
677 *Sci. Tech.* 47, 13993-14000, <https://doi.org/10.1021/es4039648>, 2013.

678 Ma, Z., Liu, R., Liu, Y., Bi, J.: Effects of air pollution control policies on PM<sub>2.5</sub> pollution improvement  
679 in China from 2005 to 2017: a satellite-based perspective. *Atmos. Chem. Phys.* 19, 6861-6877,  
680 <https://doi.org/10.5194/acp-19-6861-2019>, 2019.

681 Mann, H.B.: Nonparametric tests against trend *Econometrica: J. Econom. Soc.*, 13, 245-259, 1945.

682 Ming, L., Jin, L., Li, J., Fu, P., Yang, W., Liu, D., Zhang, G., Wang, Z., Li, X.: PM<sub>2.5</sub> in the Yangtze River  
683 Delta, China: Chemical compositions, seasonal variations, and regional pollution events. *Environ.*  
684 *Pollut.* 223, 200-212, <https://doi.org/10.1016/j.envpol.2017.01.013>, 2017.

685 Qi, J., Liu, X., Yao, X., Zhang, R., Chen, X., Lin, X., Gao, H., Liu, R.: The concentration, source and  
686 deposition flux of ammonium and nitrate in atmospheric particles during dust events at a coastal site  
687 in northern China. *Atmos. Chem. Phys.* 18, 571, <https://doi.org/10.5194/acp-18-571-2018>, 2018.

688 Qiao, X., Xiao, W., Jaffe, D., Kota, S.H., Ying, Q., Tang, Y.: Atmospheric wet deposition of sulfur and



689 nitrogen in Jiuzhaigou national nature reserve, Sichuan province, China. *Sci. Total Environ.* 511, 28-  
690 36, <https://doi.org/10.1016/j.scitotenv.2014.12.028>, 2015.

691 Qin, K., Zou, J., Guo, J., Lu, M., Bilal, M., Zhang, K., Ma, F., Zhang, Y.: Estimating PM<sub>1</sub> concentrations  
692 from MODIS over Yangtze River Delta of China during 2014-2017. *Atmos. Environ.* 195, 149-158,  
693 <https://doi.org/10.1016/j.atmosenv.2018.09.054>, 2018.

694 Quan, J., Tie, X., Zhang, Q., Liu, Q., Li, X., Gao, Y., Zhao, D.: Characteristics of heavy aerosol pollution  
695 during the 2012-2013 winter in Beijing, China. *Atmos. Environ.* 88, 83-89,  
696 <https://doi.org/10.1016/j.atmosenv.2014.01.058>, 2014.

697 Schreifels, J.J., Fu, Y., Wilson, E.J.: Sulfur dioxide control in China: policy evolution during the 10th and  
698 11th Five-year Plans and lessons for the future. *Energ. Policy* 48, 779-789,  
699 <https://doi.org/10.1016/j.enpol.2012.06.015>, 2012.

700 Shen, J., Li, Y., Liu, X., Luo, X., Tang, H., Zhang, Y., Wu, J.: Atmospheric dry and wet nitrogen  
701 deposition on three contrasting land use types of an agricultural catchment in subtropical central China.  
702 *Atmos. Environ.* 67, 415-424, <https://doi.org/10.1016/j.atmosenv.2012.10.068>, 2013.

703 Shen, J., Tang, A., Liu, X., Fangmeier, A., Goulding, K., Zhang, F.: High concentrations and dry  
704 deposition of reactive nitrogen species at two sites in the North China Plain. *Environ. Pollut.* 157,  
705 3106-3113, <https://doi.org/10.1016/j.envpol.2009.05.016>, 2009.

706 Singh, S., Sharma, A., Kumar, B., Kulshrestha, U.: Wet deposition fluxes of atmospheric inorganic  
707 reactive nitrogen at an urban and rural site in the Indo-Gangetic Plain. *Atmos. Pollut. Res.* 8, 669-677,  
708 <https://doi.org/10.1016/j.apr.2016.12.021>, 2017.

709 Tang, X.L., Fan, S.H., Du, M.Y., Zhang, W.J., Gao, S.C., Liu, S.B., Chen, G., Yu, Z., Yang, W.N.: Spatial  
710 and temporal patterns of global soil heterotrophic respiration in terrestrial ecosystems. *Earth Syst. Sci.*

711 Data 12, 1037-1051, 2020.

712 Tian, M., Wang, H., Chen, Y., Zhang, L., Shi, G., Liu, Y., Yu, J., Zhai, C., Wang, J., Yang, F.: Highly time-  
713 resolved characterization of water-soluble inorganic ions in PM<sub>2.5</sub> in a humid and acidic mega city in  
714 Sichuan Basin, China. *Sci. Total Environ.* 580, 224-234,  
715 <https://doi.org/10.1016/j.scitotenv.2016.12.048>, 2017.

716 [Vasilakos, P., Russell, A., Weber, R., Nenes, A.: Understanding nitrate formation in a world with less](#)  
717 [sulfate. \*Atmos. Chem. Phys.\* 18, 12765–12775. <https://doi.org/10.5194/acp-18-12765-2018>, 2018.](#)

718 Vrekoussis, M., Richter, A., Hilboll, A., Burrows, J., Gerasopoulos, E., Lelieveld, J., Barrie, L., Zerefos,  
719 C., Mihalopoulos, N.: Economic crisis detected from space: Air quality observations over  
720 Athens/Greece. *Geophys. Res. Lett.* 40, 458-463, <https://doi.org/10.1002/grl.50118>, 2013.

721 Wang, H., Shi, G., Tian, M., Zhang, L., Chen, Y., Yang, F., Cao, X.: Aerosol optical properties and  
722 chemical composition apportionment in Sichuan Basin, China. *Sci. Total Environ.* 577, 245-257,  
723 <https://doi.org/10.1016/j.scitotenv.2016.10.173>, 2017.

724 Wang, Q., Zhuang, G., Huang, K., Liu, T., Lin, Y., Deng, C., Fu, Q., Fu, J.S., Chen, J., Zhang, W.:  
725 Evolution of particulate sulfate and nitrate along the Asian dust pathway: Secondary transformation  
726 and primary pollutants via long-range transport. *Atmos. Res.* 169, 86-95,  
727 <https://doi.org/10.1016/j.atmosres.2015.09.013>, 2016.

728 Wang, W., Xu, W., Wen, Z., Wang, D., Wang, S., Zhang, Z., Zhao, Y., Liu, X.: Characteristics of  
729 Atmospheric Reactive Nitrogen Deposition in Nyingchi City. *Sci. Rep.* 9, 1-11,  
730 <https://xs.scihub.ltd/https://doi.org/10.1038/s41598-019-39855-2>, 2019a.

731 Wang, Y., Li, W., Gao, W., Liu, Z., Tian, S., Shen, R., Ji, D., Wang, S., Wang, L., Tang, G.: Trends in  
732 particulate matter and its chemical compositions in China from 2013–2017. *Sci. China Earth Sci.* 62,

733 1857-1871, <https://xs.scihub.ltd/https://doi.org/10.1007/s11430-018-9373-1>, 2019b.

734 Wang, Y., Li, W., Gao, W., Liu, Z., Tian, S., Shen, R., Ji, D., Wang, S., Wang, L., Tang, G.: Trends in  
735 particulate matter and its chemical compositions in China from 2013–2017. *Sci. China Earth Sci.*, 1-  
736 15, <https://xs.scihub.ltd/https://doi.org/10.1007/s11430-018-9373-1>, 2019c.

737 Wang, Y.L., Song, W., Yang, W., Sun, X.C., Tong, Y.D., Wang, X.M., Liu, C.Q., Bai, Z.P., Liu, X.Y.  
738 Influences of atmospheric pollution on the contributions of major oxidation pathways to PM<sub>2.5</sub> nitrate  
739 formation in Beijing. *J. Geophys. Res.* 124, 4174–4185, <https://doi.org/10.1029/2019JD030284>, 2019d.

740 Wei, J., Huang, W., Li, Z., Xue, W., Peng, Y., Sun, L., Cribb, M.: Estimating 1-km-resolution PM<sub>2.5</sub>  
741 concentrations across China using the space-time random forest approach. *Remote Sens. Environ.* 231,  
742 111221, <https://doi.org/10.1016/j.rse.2019.111221>, 2019.

743 Wolpert, D.H.: Stacked generalization. *Neural networks* 5, 241-259, [https://doi.org/10.1016/S0893-  
744 6080\(05\)80023-1](https://doi.org/10.1016/S0893-), 1992.

745 Xiao, Q., Chang, H., Geng, G., Liu, Y.: An ensemble machine-learning model to predict historical PM<sub>2.5</sub>  
746 concentrations in China from satellite data. *Environ. Sci. Tech.* 52, 13260-13269,  
747 <https://doi.org/10.1021/acs.est.8b02917>, 2018.

748 Xie, Y.N., Wang, G.H., Wang, X.P., Chen, J.M., Chen, Y.B., Tang, G.Q., Wang, L.L., Ge, S.S., Xue, G.Y.,  
749 Wang, Y.S., Gao, J.: Nitrate-dominated PM<sub>2.5</sub> and elevation of particle pH observed in urban Beijing  
750 during the winter of 2017 *Atmos. Chem. Phys.* 20, 5019–5033, 2020.

751 Xu, W., Liu, L., Cheng, M., Zhao, Y., Zhang, L., Pan, Y., Zhang, X., Gu, B., Li, Y., Zhang, X.: Spatial-  
752 temporal patterns of inorganic nitrogen air concentrations and deposition in eastern China. *Atmos.*  
753 *Chem. Phys.* 18, 10931-10954, <https://doi.org/10.5194/acp-18-10931-2018>, 2018a.

754 Xu, W., Zhao, Y., Liu, X., Dore, A.J., Zhang, L., Liu, L., Cheng, M.: Atmospheric nitrogen deposition in

带格式的: 缩进: 左侧: 0 厘米, 悬挂缩进: 1.5 字符, 首行缩进: -1.5 字符

带格式的: 下标

带格式的: 下标

755 the Yangtze River basin: Spatial pattern and source attribution. *Environ. Pollut.* 232, 546-555,  
756 <https://doi.org/10.1016/j.envpol.2017.09.086>, 2018b.

757 Xu, W., Zhang, L., Liu, X.J.: a database of atmospheric nitrogen concentration and deposition from  
758 the nationwide monitoring network in China. *Sci. Data* 6, 51, 2019.

759 Xue, T., Zheng, Y.X., Tong, D., Zheng, B., Li, X., Zhu, T., Zhang, Q.: Spatiotemporal continuous  
760 estimates of PM<sub>2.5</sub> concentrations in China, 2000–2016: A machine learning method with inputs from  
761 satellites, chemical transport model, and ground observations. *Environ. Interna.* 123, 345-357,  
762 <https://doi.org/10.1016/j.envint.2018.11.075>, 2019.

763 Yang, J., Kang, S., Ji, Z.: Sensitivity analysis of chemical mechanisms in the WRF-chem model in  
764 reconstructing aerosol concentrations and optical properties in the Tibetan plateau. *Aerosol Air Qual.*  
765 *Res.* 18, 505-521, doi: 10.4209/aaqr.2017.05.0156, 2018.

766 Zang, L., Mao, F., Guo, J., Wang, W., Pan, Z., Shen, H., Zhu, B., Wang, Z.: Estimation of spatiotemporal  
767 PM<sub>1.0</sub> distributions in China by combining PM<sub>2.5</sub> observations with satellite aerosol optical depth. *Sci.*  
768 *Total Environ.* 658, 1256-1264, <https://doi.org/10.1016/j.scitotenv.2018.12.297>, 2019.

769 Zhai, B.X., Chen, J.G.: Development of a stacked ensemble model for forecasting and analyzing daily  
770 average PM<sub>2.5</sub> concentrations in Beijing, China. *Sci. Total Environ.* 635, 644-658,  
771 <https://doi.org/10.1016/j.scitotenv.2018.04.040>, 2018.

772 Zhan, Y., Luo, Y., Deng, X., Chen, H., Grieneisen, M.L., Shen, X., Zhu, L., Zhang, M.: Spatiotemporal  
773 prediction of continuous daily PM<sub>2.5</sub> concentrations across China using a spatially explicit machine  
774 learning algorithm. *Atmos. Environ.* 155, 129-139, <https://doi.org/10.1016/j.atmosenv.2017.02.023>,  
775 2017.

776 Zhan, Y., Luo, Y., Deng, X., Grieneisen, M.L., Zhang, M., Di, B.: Spatiotemporal prediction of daily

777 ambient ozone levels across China using random forest for human exposure assessment. Environ.  
778 Pollut. 233, 464-473, <https://doi.org/10.1016/j.envpol.2017.10.029>, 2018a.

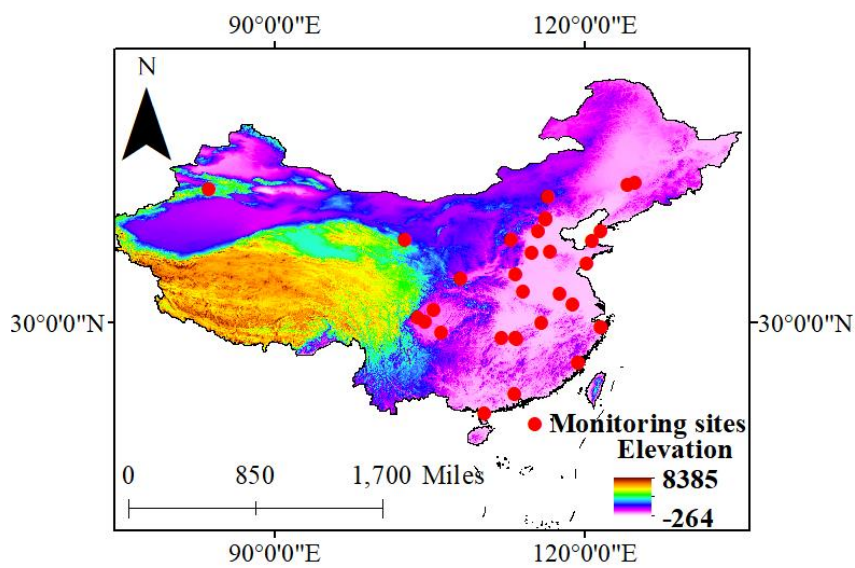
779 Zhan, Y., Luo, Y., Deng, X., Zhang, K., Zhang, M., Grieneisen, M.L., Di, B.: Satellite-Based estimates  
780 of daily NO<sub>2</sub> exposure in China using hybrid random forest and spatiotemporal Kriging model.  
781 Environ. Sci. Tech. 52, 4180-4189, <https://doi.org/10.1021/acs.est.7b05669>, 2018b.

782 Zhao, Y., Zhang, L., Chen, Y., Liu, X., Xu, W., Pan, Y., Duan, L.: Atmospheric nitrogen deposition to  
783 China: A model analysis on nitrogen budget and critical load exceedance. Atmos. Environ. 153, 32-40,  
784 <https://doi.org/10.1016/j.atmosenv.2017.01.018>, 2017.

785 Zhang, X.Y., Zhang, W.T., Lu, X.H., Liu, X.J., Chen, D.M., Liu, L., Huang, X.J.: Long-term trends in  
786 NO<sub>2</sub> columns related to economic developments and air quality policies from 1997 to 2016 in China.  
787 Sci. Total Environ. 639, 146-155, <https://doi.org/10.1016/j.scitotenv.2018.04.435>, 2018.

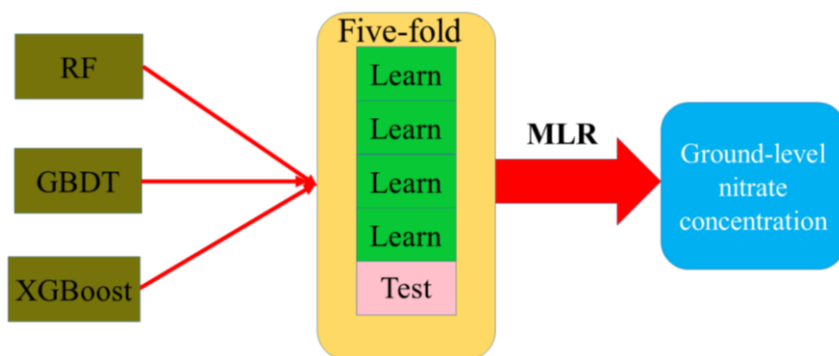
788 Zhou, K., Yang, S., Shen, C., Ding, S., Sun, C.: Energy conservation and emission reduction of China's  
789 electric power industry. Renewable and Sustainable Energy Reviews 45, 10-19,  
790 <https://doi.org/10.1016/j.rser.2015.01.056>, 2015.

791 **Fig. 1** Spatial distributions of ground-level  $\text{NO}_3^-$  monitoring sites used for model establishment. Red  
792 circles represent the ground-level sites during 2010-2015. The colormap denotes the elevation  
793 distribution across China.



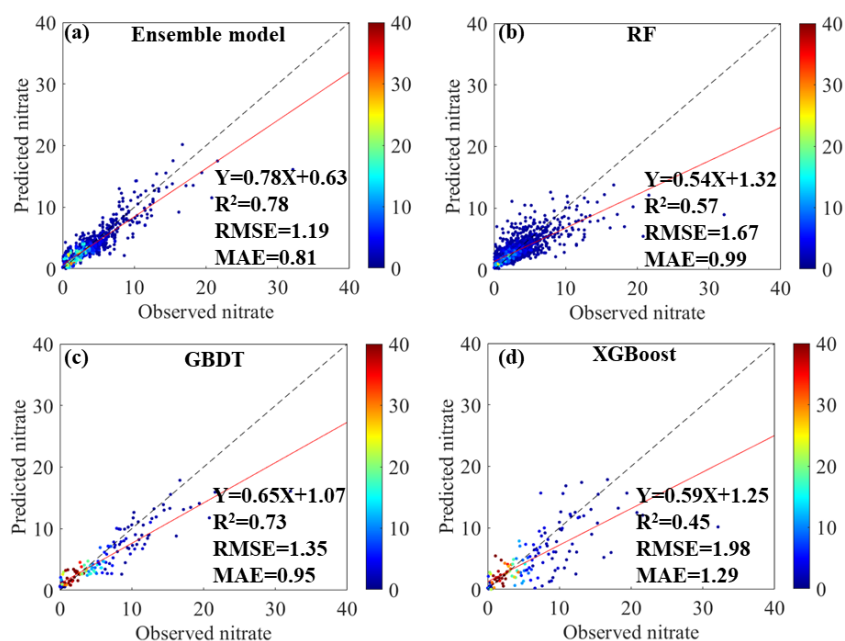
794

795 **Fig. 2** The workflow of the ensemble model development for ambient  $\text{NO}_3^-$  estimates.



796

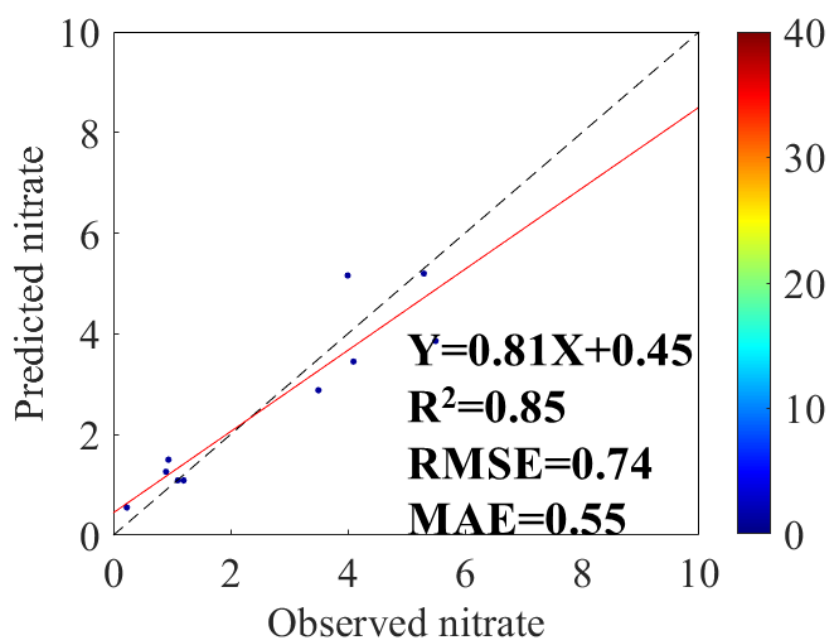
797 **Fig. 3** Density scatterplots of 10-fold cross-validation results for monthly  $\text{NO}_3^-$  estimation (Unit:  
 798  $\mu\text{g}/\text{m}^3$   $\mu\text{g N m}^{-3}$ ) across China for the ensemble decision trees model (a), RF (b), GBDT (c), and  
 799 XGBoost (d), respectively. The color bar reflects the sampling size of each model. The red solid line  
 800 denotes the best-fit line through the data points (1636 points). The black dashed line denotes the  
 801 diagonal, which could be used to reflect the deviation of data points.



802

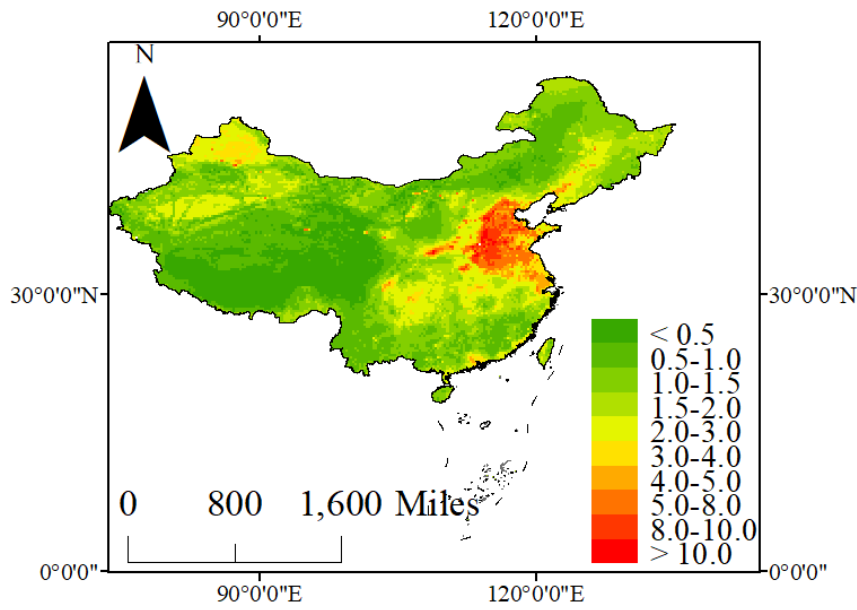


803 **Fig. 4** The transferability validation of the ensemble model in estimating  $\text{NO}_3^-$  concentration over  
804 China based on the unlearning observation data (Shen et al., 2013; Shen et al., 2009; Wang et al.,  
805 2019a; Xu et al., 2018b). The color bar reflects the sampling size of each model. The red solid line  
806 denotes the best-fit line through the data points. The black dashed line denotes the diagonal, which  
807 could be used to reflect the deviation of data points.



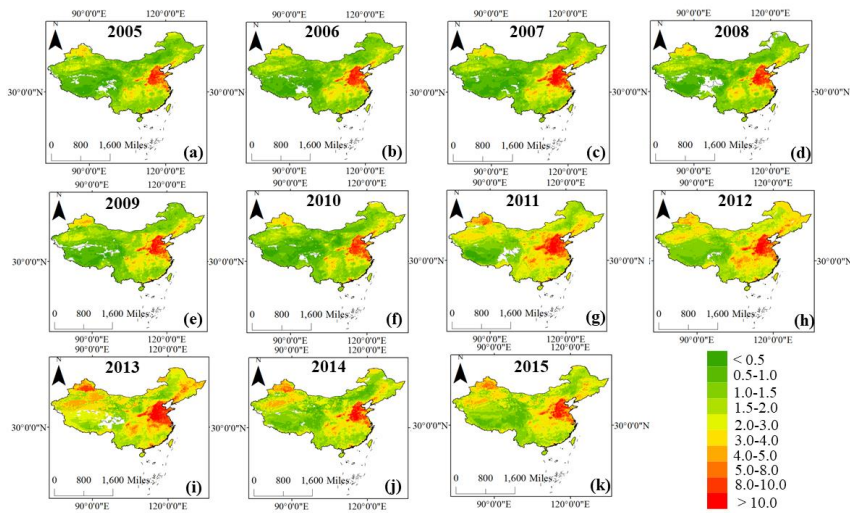
808

809 **Fig. 5** The spatial pattern of estimated  $\text{NO}_3^-$  concentration ( $\mu\text{g}/\text{m}^3$   $\mu\text{g N m}^{-3}$ ) over China during  
810 2005-2015 based on the ensemble model.



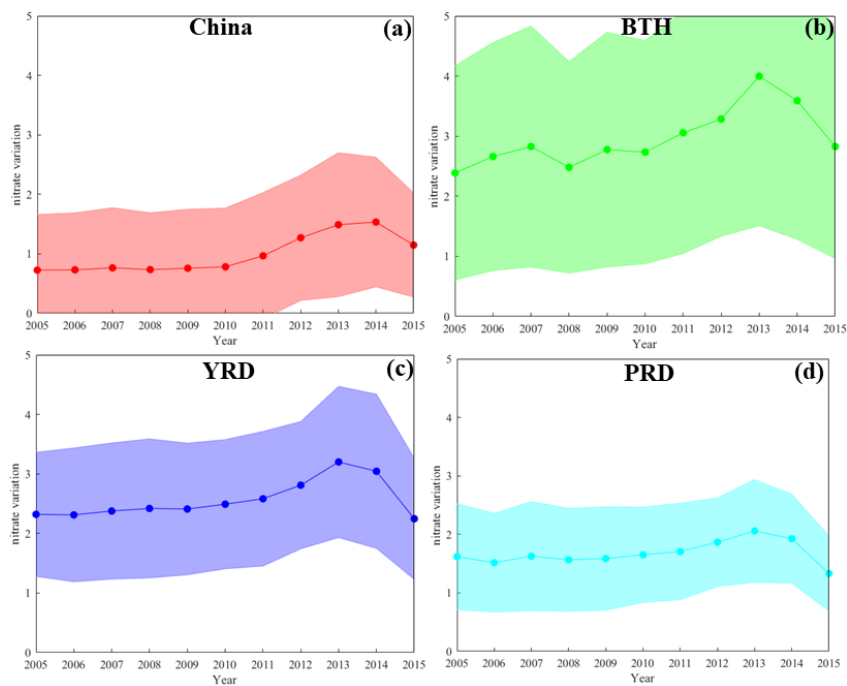
811

812 **Fig. 6** The annual mean predicted  $\text{NO}_3^-$  concentrations ( $\mu\text{g}/\text{m}^3$   $\mu\text{g N m}^{-3}$ ) across the entire China  
813 from (a)-(k) 2005-2015 based on the ensemble model.



814

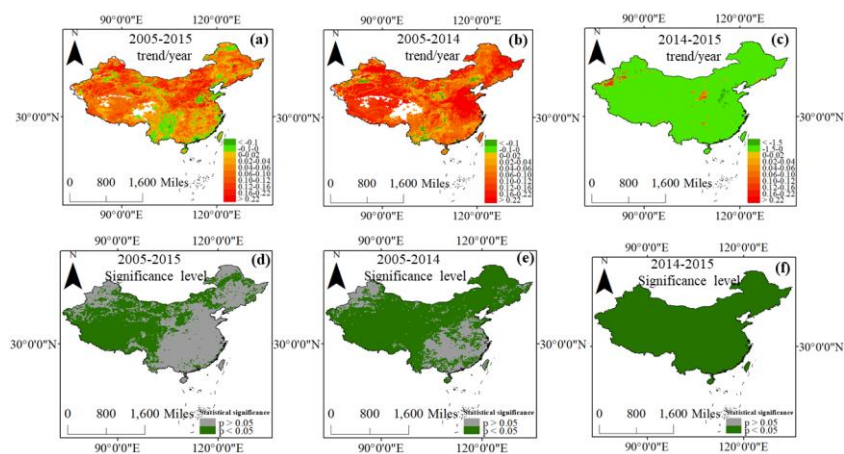
815 **Fig. 7** The annual mean  $\text{NO}_3^-$  concentrations in major regions across China during 2005-2015. The  
816 solid lines denote the mean  $\text{NO}_3^-$  concentrations and the shadow represents the range of  $\text{NO}_3^-$   
817 concentrations.



818

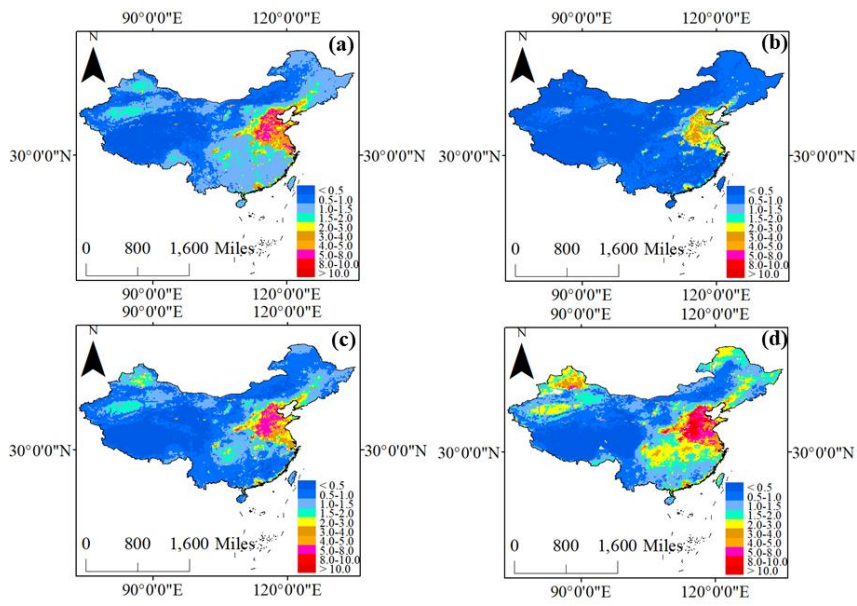
819

820 **Fig. 8** The long-term trends of  $\text{NO}_3^-$  concentrations ( $\mu\text{g N m}^{-3}$ ) and significance levels in China (a,  
 821 b, and c denote the annual variation of ambient  $\text{NO}_3^-$  concentration during 2005-2015, 2005-2014,  
 822 and 2014-2015, respectively. d, e, and f represent the significance level of  $\text{NO}_3^-$  trend during these  
 823 periods). The pale green color denotes the regions with the significant variation of ambient  $\text{NO}_3^-$   
 824 concentrations ( $p < 0.05$ ), while the gray color represents the regions with insignificant variation of  
 825  $\text{NO}_3^-$  concentrations.



826

827 **Fig. 9** The mean concentrations of ambient  $\text{NO}_3^-$  in spring (a), summer (b), autumn (c), and winter  
828 (d) during 2005-2015 over China, respectively.



829

830 **Table 1** The cross-validation result of NO<sub>3</sub><sup>-</sup> estimation over China during 2010-2015.

<u>SeasonYear</u>	Sample size	R <sup>2</sup> value	Slope	RMSE ( <u>µg/m<sup>3</sup>µg N m<sup>-3</sup></u> )	MAE ( <u>µg/m<sup>3</sup>µg N m<sup>-3</sup></u> )
2010	135	0.62	0.60	1.39	0.90
2011	291	0.88	0.85	0.32	0.24
2012	274	0.89	0.86	0.33	0.28
2013	312	0.83	0.82	0.64	0.43
2014	306	0.74	0.76	1.50	1.04
2015	318	0.78	0.78	1.35	0.86

831

832 **Table 2** The cross-validation result of NO<sub>3</sub><sup>-</sup> estimation over China in four seasons.

Season	Sample size	R <sup>2</sup> value	Slope	RMSE ( $\mu\text{g}/\text{m}^3$ $\mu\text{g N m}^{-3}$ )	MAE ( $\mu\text{g}/\text{m}^3$ $\mu\text{g N m}^{-3}$ )
Spring	395	0.80	0.80	0.71	0.48
Summer	418	0.85	0.84	0.29	0.20
Autumn	437	0.80	0.78	1.10	0.70
Winter	386	0.75	0.73	1.85	1.23

833



834 **Table 3** The cross-validation result of NO<sub>3</sub><sup>-</sup> estimation over China in different regions (Northeast  
 835 China includes Heilongjiang, Jilin, and Liaoning provinces; NCP includes Beijing, Tianjin, Hebei,  
 836 Henan, Shandong, and Shanxi provinces; Southeast China includes Jiangsu, Zhejiang, Fujian,  
 837 Guangdong, Jiangxi, Anhui, Hunan, Hainan, Shanghai, and Hubei provinces; Southwest China  
 838 includes Yunnan, Guangxi, Sichuan, Tibet, Chongqing, and Guizhou provinces; Northwest China  
 839 includes Inner Mongolia, Xinjiang, Gansu, Qinghai, Ningxia, and Shaanxi.

Season	Sample size	R <sup>2</sup> value	Slope	RMSE ( $\mu\text{g}/\text{m}^3$ )	MAE ( $\mu\text{g}/\text{m}^3$ )
Northeast	175	0.44	0.43	1.30	0.81
China					
NCP	492	0.70	0.64	1.74	1.06
Southeast	395	0.59	0.57	1.50	0.84
China					
Southwest	384	0.60	0.59	2.08	1.41
China					
Northwest	190	0.58	0.52	2.06	1.38
China					

840

841 **Table 4** The trend analysis of NO<sub>3</sub><sup>-</sup> concentrations in China, BTH, YRD, and PRD regions during  
 842 2005-2015.

Period	Trend	China	BTH	YRD	PRD
2005-2014	Trend ( $\mu\text{g}/\text{m}^3 \mu\text{g N}$ $\text{m}^3/\text{year}$ )	0.08	0.13	0.08	0.03
	Significance	p < 0.05	p < 0.05	p < 0.05	p < 0.05
2014-2015	Trend ( $\mu\text{g}/\text{m}^3 \mu\text{g N}$ $\text{m}^3/\text{year}$ )	-0.40	-0.76	-0.79	-0.59
	Significance	p < 0.05	p < 0.05	p < 0.05	p < 0.05
2005-2015	Trend ( $\mu\text{g}/\text{m}^3 \mu\text{g N}$ $\text{m}^3/\text{year}$ )	0.04	0.04	-0.01	-0.03
	Significance	p < 0.05	p > 0.05	p > 0.05	p < 0.05

843

844

845